SIMULINK SIMULATION OF AN AIRGAPLESS MOTOR

A Thesis

Submitted to the Faculty

of

Purdue University

by

Chuyue Tang

In Partial Fulfillment of the

Requirements for the Degree

of

Master of Science in Electrical and Computer Engineering

December 2018

Purdue University

Indianapolis, Indiana

THE PURDUE UNIVERSITY GRADUATE SCHOOL
STATEMENT OF COMMITTEE APPROVAL

Dr. Euzeli Cipriano Dos Santos, Chair

      Department of Electrical and Computer Engineering

Dr. Brian King

      Department of Electrical and Computer Engineering

Dr. Lingxi Li

      Department of Electrical and Computer Engineering

Approved by:

      Dr. Brian King

          Head of the Graduate Program

ACKNOWLEDGMENTS

This research was supported by department of Electrical and Computer Engineering. I thank my mentor, Dr. Dos Santos who provided insight and expertise that greatly assisted the research and my friends, Maryam, Omar, Rishikesh and Nathan for the assistance during my research. I would also thank Dr. King for being so encouraged. Especially thank Dr. Li and Sherrie Tucker for all the assistance! I would not be me without you and I appreciate you all.

I would also like to thank my parents for being there for me no matter what. They have been giving me great strength to concur all the challenges in my life and being grateful as in all time!

I hope the contents in this thesis will give these outstanding scholars some new ideas.

PREFACE

This thesis explores the control strategies of an air-gapless motor. Air-gapless motor is a brand new kind of motor in the industry and still needs many excellent researchers who are willing to dedicate their time to it and make breakthroughs.

TABLE OF CONTENTS

LIST OF TABLES

LIST OF FIGURES

ABBREVIATIONS

EMF	Electromagnatic field
ECM	Equivalent circuit method
NA	Numerical analysis
ANSYS	ANSYS simulation solutions
LUT	Look-up table
FEM	Finite element method
PWM	Pulse width modulation

ABSTRACT

Tang, Chuyue. M.S.E.C.E., Purdue University, December 2018. Simulink Simulation of an Airgapless Motor. Major Professor: Euzeli Cipriano Dos Santos Jr.

Nowadays, electrical motors are widely used in the automotive industry because of their high efficiency and lossless characteristics. One downside is that the system is complicated to control and it requires more complex control strategies. Moreover, compared to other motors, electrical motors produce less torque, which limits its capability.

Therefore, in this thesis, an air-gapless electric motor is presented. Instead of having a static air gaps between the rotor and the stator, the gap changes dynamically creating contact which generates higher torques. A SIMULINK simulation method is used for this motor in order to show the systems dynamic behaviors.

Five blocks are used in the system: the block to find phase currents, the block to find phase torque, the block to find self-inductance, the block to obtain mechanical speed of the motor and the block to simulate the saturation effect. These blocks are developed based on the analytical relationships between components, which are shown in Chapter two.

Moreover, saturation effect in the iron cores is taken into consideration in this thesis due to the fact that it always effects the shape of the magnetic field curves. And four different materials are discussed and compared in Chapter three. The findings in this chapter is that carbon steel and silicon steel serve as better materials of the rotor in the air-gapless motor than soft ferrite and nickel steel because they tend to have higher torques under same levels of the currents and they have larger torque stability regions.

As for Chapter four, a current control strategy is proposed with an inverter, this could simulate the current controller in a real application. Trial and error PID controller tuning method is discussed in Chapter four.

1. INTRODUCTION

The objective of this thesis is to present dynamic analysis of an air-gapless motor using SIMULINK. This thesis is divided into five chapters. The first chapter will introduce a comprehensive review of advantages and disadvantages of electrical motors with emphasis on motors with external rotor. The second chapter proposes a solution in SIMULINK environment in which five blocks are proposed to define the crucial components in the motor such as self-inductance, electrical torque and mechanical speed. The third chapter will focus on the discussion when a saturation effect of the iron core is considered in motor. The fourth chapter deals with a current controller as well as a three-phase three-leg inverter. A PWM strategy is used to generate gate signals of the inverter. The final chapter will be a summary that goes over the above.

1.1   External Rotor Based Electric Motors

Among two major types of motors (hydraulic motors and electric motors), compared to electrical motors, hydraulic motors are more reliable, well suited for a wide range of higher force applications while electrical motors are limited to some environments. Hydraulic motors are more flexible because of their structures while electric motors will be more limited.

In addition, electrical motors have torque density limitations, which is why they haven't been considered as competitive as hydraulic motors in the last ten years. Torque density ($ft - lbs$ of motor torque developed per lb of motor mass) is the key to define metric. For example, liquid-cooled permanent magnet (PM) motors have the torque density of 8 $ft - lbs$, advanced PM motors and high temperature superconductivity motors have more than 16 $ft - lbs$. However, none of liquid-cooled permanent

magnet motors, advanced PM motors or high temperature superconductivity motors give torque density that could be compared to hydraulic motors.

On the other hand, hydraulic motors face some problems that electric motors do not have. First of all, they present a range of 6 percent to 40 percent rate of efficiency which is not as high as electrical motors. Secondly, hydraulic motors have a rather complex braking system when applied thus they could be more difficult to control compared to electric motors.

Electrical motors are widely used in the automotive market and there are two categories of these motors which are well-known, external motors as well as internal motors.

External motors refer to the motors when the rotor is outside the stator. Internal motors refer to when rotors are inside stators. An external motor is presented in this thesis. Advantages of external motors include a decreasing flux leakage due to the larger area for stator slots, which will protect the motor from a heat loss with the assistance of the fan. Other advantages would be: 1) since the hub and impeller are an integrated unit of the short axial on an external motor, the motor is precisely balanced [1], 2) applying low voltage variation to the external motor makes speed control possible to access [2], 3) space saving due to the external rotor principle, making it ideal for some limited space equipment, 4) creates higher torque density, lower rotating inertia which are essential requirements for some applications, such as in-wheel automotive applications [3] when motors are installed next to the drive wheels.

1.2 Discussion of Traditional Air Gaps

The air gap is one of the essential components when it comes to electrical motor designs. In common applications, rotors and stators are not allowed to touch each other to avoid damage on both stator and rotor, so that to avoid mechanical deflection and losses in the supporting bearings. Therefore, the air gaps shall be large enough

to overcome shaft stiffness due to the unbalanced magnetic field and to prevent the rotor from striking the stator. Therefore to avoid unsatisfied effects.

However, in order to reach a higher efficiency of electromagnetic devices, a lower resistance to the passage of field flux provided by the magnetic materials is required. Air usually has a higher resistance to magnetic flux than the materials used for design, therefore, it will produce more electrical loss.

Plenty of papers have discussions about how critical it is to design around air gaps. The common calculation methods involve 1) rotor peripheral speed, 2) core stack length and 3) rotor peripheral speed. Moreover, calculation of the air gaps are significantly affected by the characteristics of the motor and its applications.

For instance, when applied to DC machines, the AC field created by the armature winding and distortion supplied by the DC field are affected by the air gaps. (stationary magnetic field in the synchronous machine, rotating magnetic field in the DC machine) Thus causes "armature reaction". Hence, in order to reduce this undesired effect, for these machines, they are more likely to have larger air gaps than other machines in the industry.

Another example would be seen in the design in a 100 to 750 kilowatts induction motor, typical air gaps are designed to be 0.2 to 5mm [4]. For induction motors, gaps are directly proportional to the leakage flux and the inversely proportional to the mutual flux, therefore, the larger the air gap, the less the rotor EMF, current, and electric torque. Moreover, the higher the motor speed, the larger the gaps.

As for synchronous machines, field windings are separated from the magnetic field, which means the EMF is dynamically induced due to relative motion between the field and conductors instead of inducing from the mutual induction. Thus, air gaps have a limited impact on the process [5]. Therefore in the cases of synchronous machines, it is more likely to have smaller air gaps to match their particular requirements.

In addition, large air gaps could also force the flux path through the surrounding structure of the machine such as the yoke, causing energy losses called "the flux fringing effect". Obviously, it is an unwanted phenomenon which may lead to the

increased proximity and eddy current loss of the conductors. The eddy effect is an effect happens in the magnetic materials according to Faraday's law of induction. As the coil generates an electromagnetic field when AC currents are injected, it will also cause magnetically induced circular electric currents in a metal sheet [6]. The eddy effect may also lead to a heat generation from the metal sheet in which may reduce the efficiency of the energy transmission in motors.

In other cases, the gaps are not necessarily only composed of air but with water, plastic, wood or even vacuum. Gaps could also take different forms and shapes. These are dependent on the applications. However, it is worth mentioning that no matter how dynamic they could be, gaps must be as uniform as possible or in a regular changing rate.

A non-uniform gap will cause increased noise as well as vibration [7]. So normally in a motor, it is common to have a uniform air gap to keep the variation limited to positive or negative 10 percent as most [8].

As for other applications, such as relays, as the device facilitates moving between the fixed part and the active part, air gap allows for electrical contact of the relay. However, in transformers, air gaps are seen as an undesirable component for the role of the transformer is to deliver the energy between windings, so the loss caused by air gaps need to be completely avoided [3].

1.3   Motion of the Motor

In the air-gapless external motor, the rotation of the motor is shown in Fig. 1.1, the stator is always run in the same direction to the rotor but in different speeds. Therefore the movements of the motor will induce the friction and slight strikes between the stator and the rotor in real experiments.

As the motor is running, air gaps are changing from the zero to the difference between the radius of the stator and rotor. It is worth to note that gaps are not exactly zero to simulate the situation of the contact between stator and rotor because
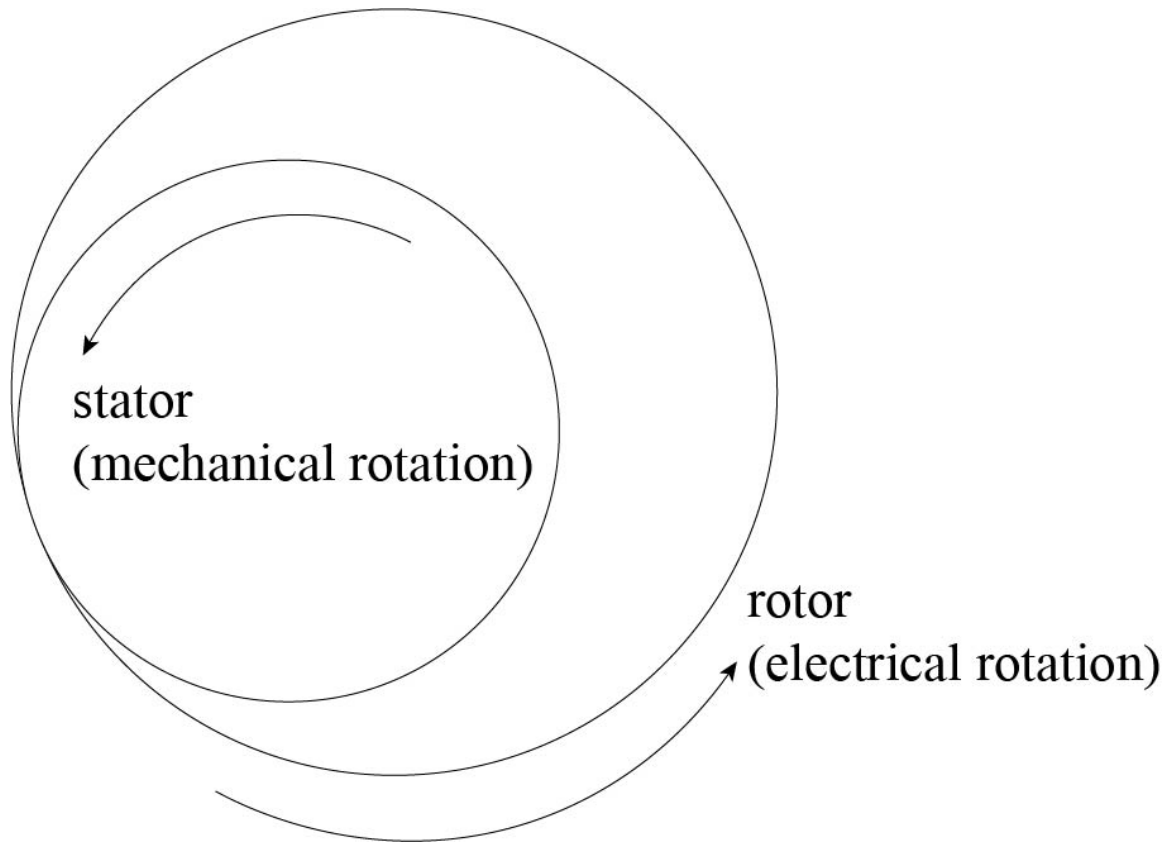
Fig. 1.1. This figure shows the rotating direction of the motor

of the roughness of the materials which will leave invisible air gaps between the stator and the rotor as shown in Fig. 1.2. It is obvious that these gaps consist of two main parts, bulges and sunk parts as shown in the figure. These uneven distributions exist but these distributions are hard to be recognized thus could be neglected as the motor is running. And if air gap is minimized, then a maximized force could be observed accordingly.

From Fig. 1.3, the movement of the motor is observed from the top view. Fig. 1.3 shows the motor moves counterclockwise and the rotor contacts the stator in different positions.

As the motor running, the angle of the touching point between the stator and the rotor is θ and it is shown in Fig. 1.4.

sunk part   *bulge*
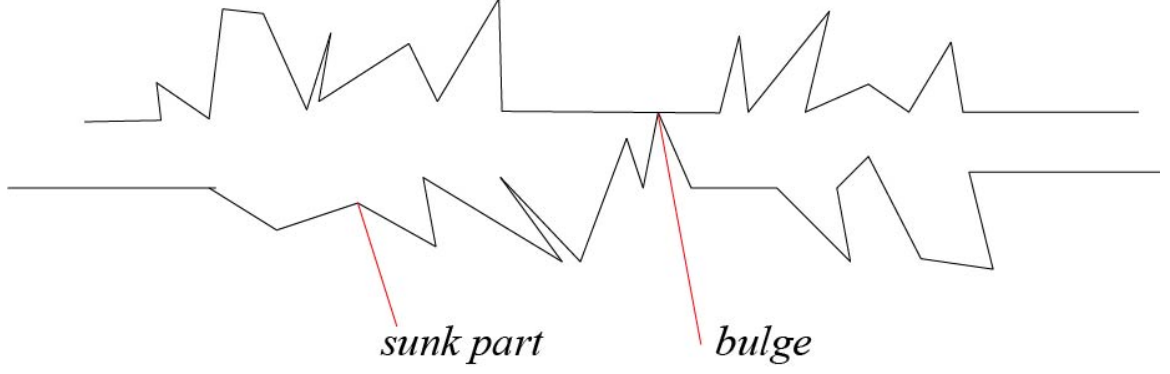
Fig. 1.2. This figure shows the invisible air gaps between the stator and the rotor
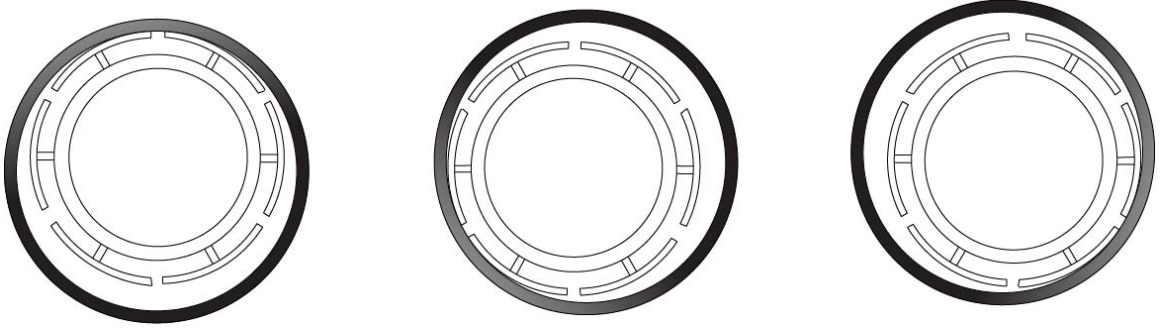
Fig. 1.3. This is the possible positions of the motor

Gaps between these two components are cosine functions, which indicate the position of the stator and the rotor and these gap functions change along the motor movements. r_1 is the radius of the stator and r_2 is the radius of the rotor. To better show the relationships of the gaps and the angles, Fig. 1.4 is scaled to facilitate the visualization. From the geometrical laws, gap functions are obtained as following:

$$g(\Theta) = r_2 - r_{21}\cos(\Theta) - \sqrt{r_1^2 - r_2^2\sin^2(\Theta)} \tag{1.1}$$

Where,

$$r_{21} = r_2 - r_1 \tag{1.2}$$
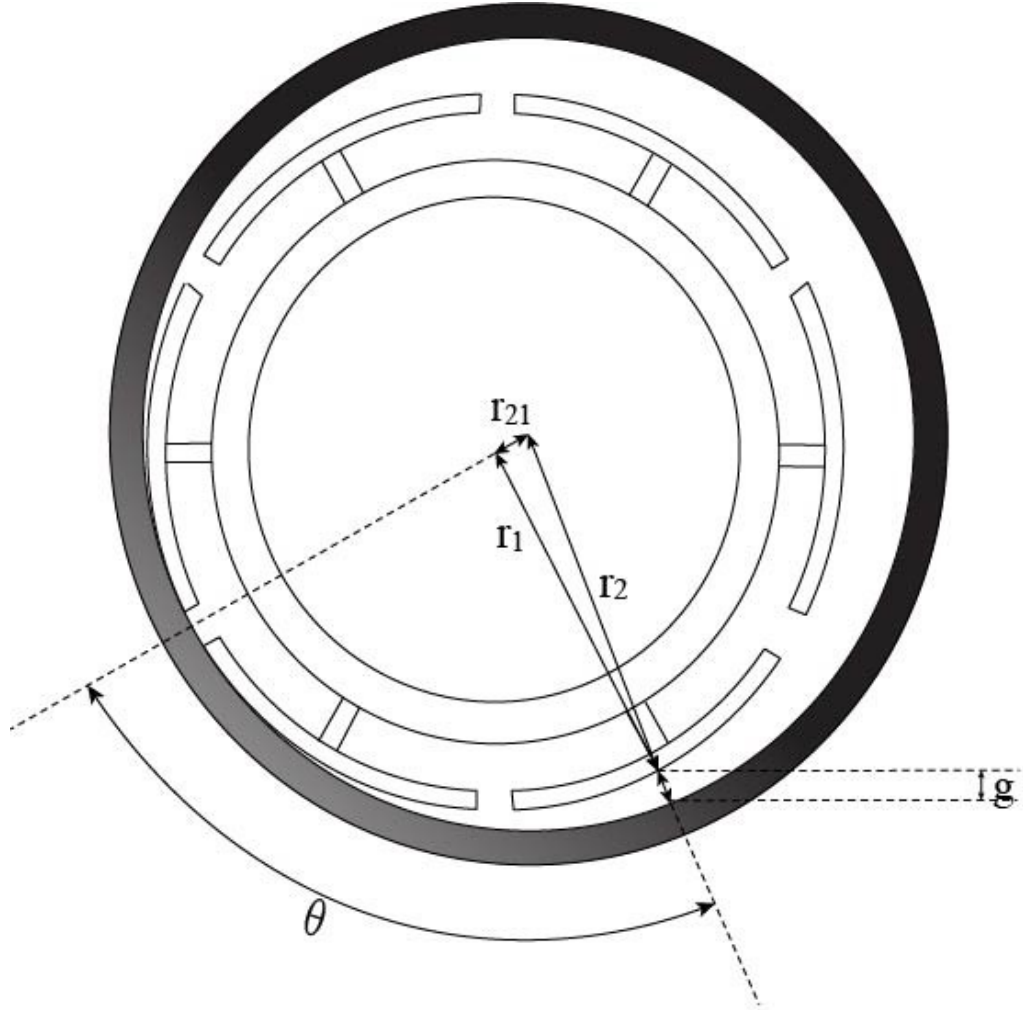
Fig. 1.4. The possible positions of the motor

And since r_1 and r_2 are close to each other in this case, then r_{21} is approximately equals to zero, therefore, the above equation could be simplified as following:

$$g(\Theta) = r_{21}[1 - \cos(\Theta)] \tag{1.3}$$

Accordingly, there are six positions of interest in terms of gap measurements $(g_{1a}, g_{2a},$ etc.) , which are:

$$g_{1a}(\Theta) = r_{21}[1 - \cos(\Theta - \pi/6)] \tag{1.4}$$

$$g_{1b}(\Theta) = r_{21}[1 - \cos(\Theta + \pi/6)] \tag{1.5}$$

$$g_{2a}(\Theta) = r_{21}[1 - \cos(\Theta + 3\pi/6)] \tag{1.6}$$

$$g_{2b}(\Theta) = r_{21}[1 - \cos(\Theta + 5\pi/6)] \tag{1.7}$$

$$g_{3a}(\Theta) = r_{21}[1 - \cos(\Theta + 7\pi/6)] \tag{1.8}$$

$$g_{3b}(\Theta) = r_{21}[1 - \cos(\Theta + 9\pi/6)] \tag{1.9}$$

Equivalent circuit method is commonly used in researches. The advantages are vary, such as equivalent circuit method requires the deconstruction of the circuit into ideal simple circuit elements so it could simplify the situation and obtain the instant relationships among components.

Fig. 1.5 shows the equivalent circuit of the motor, where R_s, R_r are the reluctances of the stator and the rotor which are constants. And R_1a, R_1b are the reluctance from the air gaps, which are functions along with the movements of the motor. The equations of the reluctance are shown in Chapter two.

Fig. 1.5. This figure shows the equivalent circuit of the motor

phase current injected
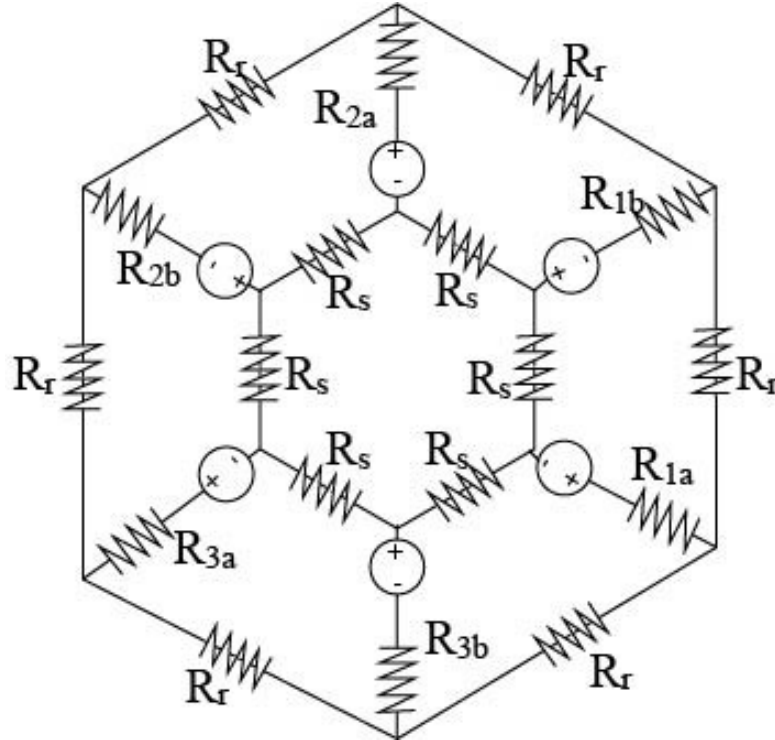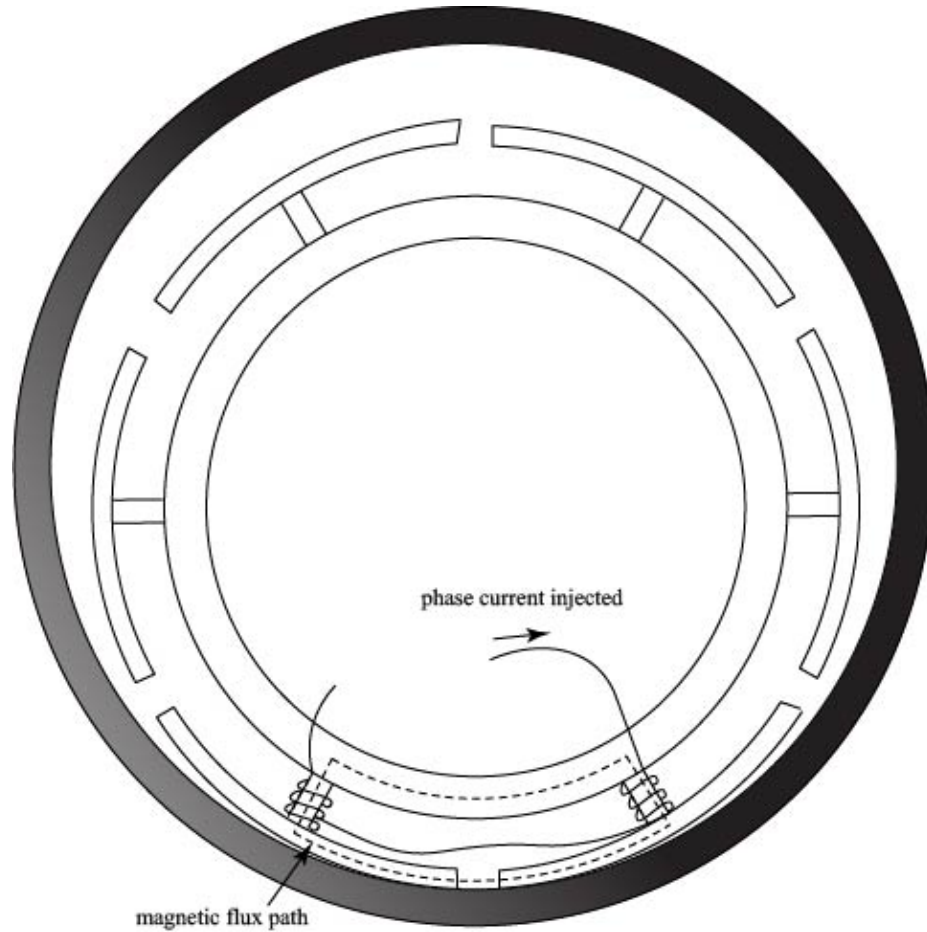
magnetic flux path

Fig. 1.6. This figure shows the flux path in the motor

To have steady movements of the motor, the number of magnetic bi-poles could not be less than three. The bi-poles will excite magnetic field for each pole pairs that have two teeth. For one of those two towards to north and the other one towards to south, which indicates a C-core construction as it is shown in Fig. 1.6.

Flux linkage is induced when the phase currents are injected to the coils and it mainly flows along the iron cores since air gaps have low conductivity and much more resistance. An equivalent circuit of flux linkage is shown in Fig. 1.7, which indicates fluxes from each poles and from one pole to the next pole. Moreover, the relationships among the different kinds of fluxes in Fig. 1.7 is shown in the matrix in section 2.1.

2. DYNAMIC SIMULATION OF AN AIR-GAPLESS MOTOR

Motor control strategies are fairly complicated because of the dynamic factors in one system, that is why in majority of cases motion sensors are essential to the analysis. Such factors could be the intriguing voltages, the movements and the forces during the movements and materials [9]. By using MATLAB-SIMULINK method, setting up analytical blocks could make motor control easier due to the advantages that SIMULINK has, such as being able to build up function blocks, having fairly large power electronic library and being able to run the system spontaneously. By using SIMULINK simulation, plenty of control Strategies could be taken into consideration such as current control strategies, hysteresis current control method [10] and since electric motors are broadly used in industry and researches, there are plenty of papers demonstrate current control loops [11] [12] [13] [14].

Other studies suggest that by controlling the currents can reduce current ripple and maintain the rated values of the torque at the same time [15] and SIMULINK provides this probability a better environment to compile and run more easily.

A table of parameters that have been used in this paper is presented below.

Table 2.1.: Parameters Used in the Simulation.

Parameter	Description	Value
B_m	Coefficient of friction	0.1
J_m	Moment of inertia	0.01 $(kg.m^2)$
V_{dc}	DC-link voltage	20 (V)
μ_0	Permeability of air	4π x $10^{-7}(H/m)$
		Continued on next page

Table 2.1 – continued from previous page

Parameter	Description	Value
μ_s	Relative permeability of the stator	2000
l_s	Length of the flux path in the stator	0.1 (m)
l_r	Length of the flux path in the rotor	0.07 (m)
A_s	Cross-sectional area of the stator	140 x $10^{-6}(m^2)$
A_r	Cross-sectional area of the rotor	25 x $10^{-5}(m^2)$
N	Number of turns in each tooth	160
r	Series resistance in each winding	3 (Ω)
R_s	Stator radius	0.0953(m)
R_r	Rotor radius	0.096 (m)
f_e	Electrical frequency	2 (Hz)
T_{load}	Load torque	0.1 (N.m)

2.1 Block Diagram Representation to Obtain Phase Currents

Block diagrams are used to model situations in the system including the behaviors of the motor when saturation happens, the system could be simulated in SIMULINK or another software such as C or C++ [16]. SIMULINK blocks have multiple parameters which could be used as inputs at the same time and MATLAB-SIMULINK simulation method is especially useful in the motor analysis because of the complexity of motor control. An assumption was mentioned in [17] is used as basis for these simulation blocks presented in this thesis.

In the simulation, there are five block diagrams: 1) the block diagram representation to obtain phase currents in the system, 2) the block diagram representation to obtain self-inductances, 3) the block diagram representation to obtain phase torque, 4) the block diagram representation to obtain electrical torque as well as shows the

relationship between the torque and mechanical speed, and last but the least, 5) the saturation block diagram representation which will also be discussed in Chapter three.

It is known that the derivation for phase currents in a traditional way is related to phase voltages and self-inductances. For this air-gapless motor, it is excited by the currents coming from a bi-pole configuration as it is shown in Fig. 2.1. Both pole A and pole B constitute the configuration of phase one. Currents i_1 goes to the windings of pole A and pole B. λ_{1a} and λ_{1b}.
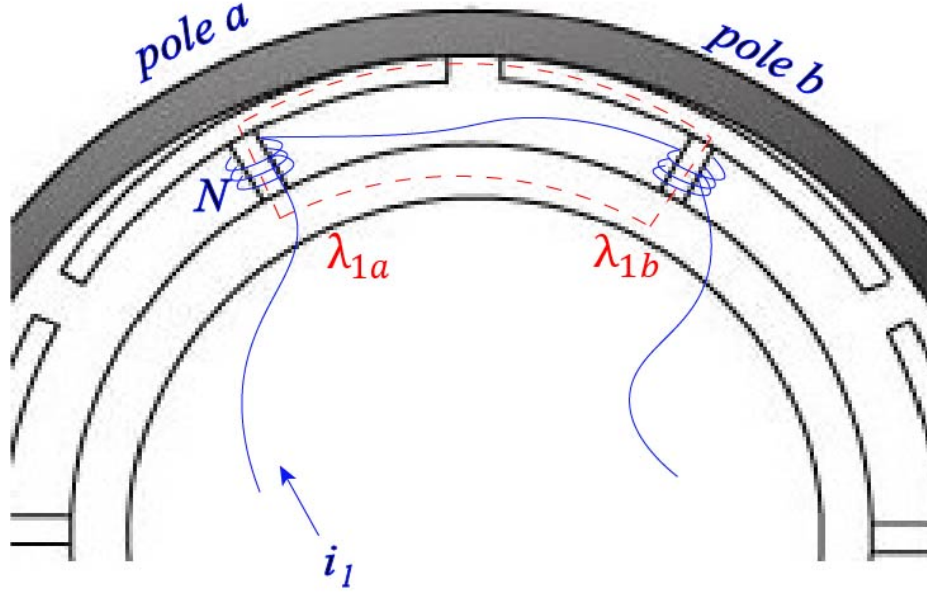
Fig. 2.1. Bi-pole of phase one highlighted with windings and flux path

According to the Maxwell's electromagnetic theory, i_1 in the windings produces magnetic flux linkage, phase voltages and phase currents have a relationship which is shown in Equ. 2.1 to Equ. 2.3.

$$v_1 = r_1 i_1 + \frac{d\lambda_{1a}}{dt} + \frac{d\lambda_{1b}}{dt} \tag{2.1}$$

$$v_2 = r_2 i_2 + \frac{d\lambda_{2a}}{dt} + \frac{d\lambda_{2b}}{dt} \tag{2.2}$$

$$v_3 = r_3 i_3 + \frac{d\lambda_{3a}}{dt} + \frac{d\lambda_{3b}}{dt} \tag{2.3}$$

From Equ. 2.1 - 2.3, the derivative is expressed as accumulation in block diagram. Where,

$$L_{1a1a} = N(\lambda_{1a} + \lambda_{1b})/i_1 \tag{2.4}$$

$$L_{2a2a} = N(\lambda_{2a} + \lambda_{2b})/i_2 \tag{2.5}$$

$$L_{3a3a} = N(\lambda_{3a} + \lambda_{3b})/i_3 \tag{2.6}$$

And,

$$\lambda_{1a} = \lambda_{1b} \tag{2.7}$$

$$\lambda_{2a} = \lambda_{2b} \tag{2.8}$$

$$\lambda_{3a} = \lambda_{3b} \tag{2.9}$$
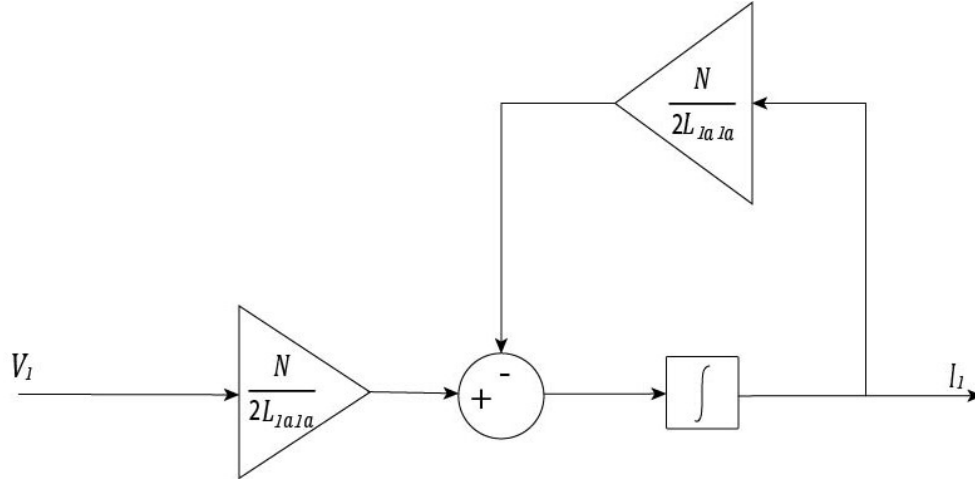
Fig. 2.2. Phase current model

Phase current i_1 thus could be obtained from Equ. 2.1 - 2.9. In the Fig. 2.2, v_1 is the phase voltage injected to the system and i_1 is the phase current accordingly. L_{1a1a} is the self-inductance of phase one and R is the resistance of the cores which is a constant given by the conduct material, the crossing area and the length of the resistance.

2.2   Block Diagram Representation to Obtain Self-inductance

The magnetic field will be composed of both self-inductance and mutual-inductance. Since copper loss is one of the losses of the motor, iron loss and mechanical loss and these losses is small enough to be neglected [15]. Therefore, flux leakage in the system is neglected due to the limited dimensions of the motor.
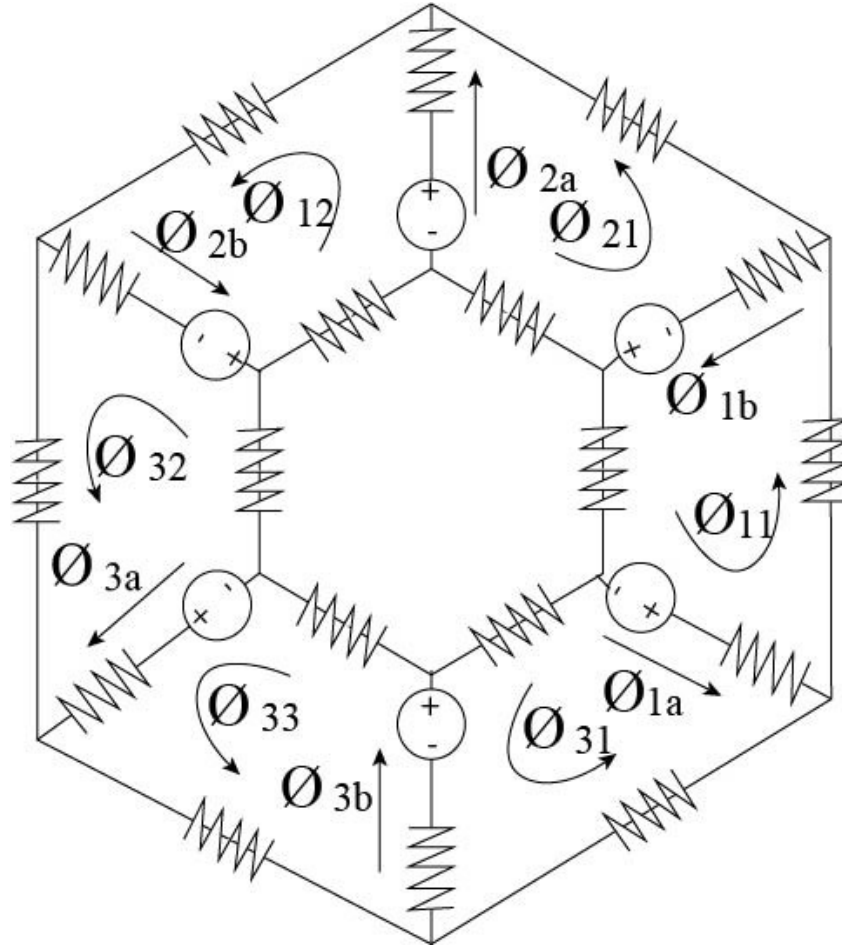
Fig. 2.3. This figure shows the equivalent circuit of the motor

Fluxes are shown in Fig. 2.3 have relationships which could be expressed as the following matrix:

$$
\begin{bmatrix} \phi_{1a} \\ \phi_{1b} \\ \phi_{2a} \\ \phi_{2b} \\ \phi_{3a} \\ \phi_{3b} \end{bmatrix}
=
\begin{bmatrix}
1 & 0 & 0 & -1 & 0 & 0 \\
1 & 0 & 0 & 0 & -1 & 0 \\
1 & 0 & 0 & 0 & -1 & 0 \\
1 & 0 & 0 & 0 & -1 & 0 \\
1 & 0 & 0 & 0 & -1 & 0 \\
1 & 0 & 0 & 0 & -1 & 0
\end{bmatrix}
\begin{bmatrix} \phi_{11} \\ \phi_{22} \\ \phi_{33} \\ \phi_{31} \\ \phi_{21} \\ \phi_{32} \end{bmatrix}
\tag{2.10}
$$
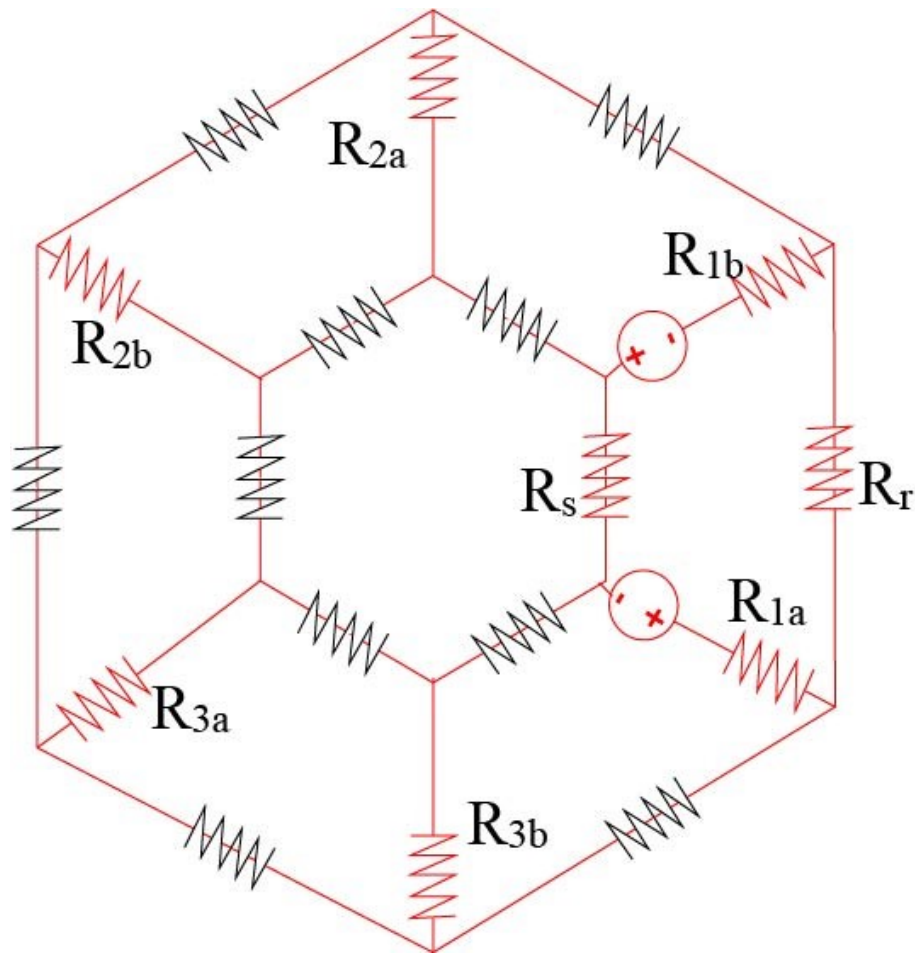
Fig. 2.4. This figure shows the equivalent circuit of the motor to calculate self inductance

In Fig. 2.3, for instance, ϕ_{1a} is the flux that generated by i_1 on the pole A, ϕ_{1b} is the flux that generated by i_1 on the pole B, ϕ_{11} is the flux that generated between pole A and pole B of phase one and ϕ_{31} is the flux that generated between pole A of phase one and pole B of phase three.
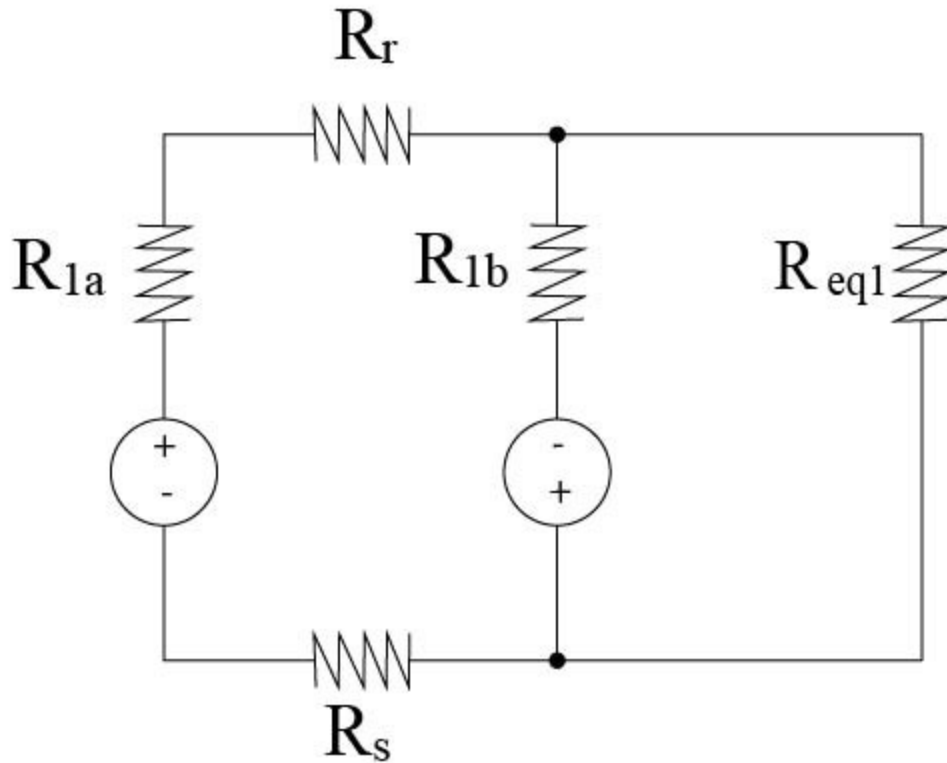
Fig. 2.5. This figure shows the equivalent circuit of the motor to calculate self inductance

Both self-inductance and mutual-inductance are essential concepts for an electrical motor and inductances come from flux linkage of the motor. The relationship between these two can be found from Equ. 2.4 - 2.6.

Self inductance is defined as the induction of a voltage in a current-carrying wire when the current in the wire itself is changing. According to Lenz's law mutual inductance refers to the fact that a change in the current of one coil has impact on

the current and voltage in the second coil. Thus for example, L_{1a1a} is self-inductance and L_{1a2b} is mutual inductance, etc.

To obtain self-inductance and mutual inductance, Fig. 2.4 shows the equivalent circuit of gaining self-inductance and Fig. 2.5 shows the simplified equivalent of gaining self-inductance. From Fig. 2.4 and Fig. 2.5, self-inductance is obtained by the following equations:

$$L_{1a1a} = N\phi_{1a}/(i_1) = N^2/((R_{1a} + R_{1b} + R_r + R_s)//R_{eq1}) \tag{2.11}$$

where,

$$R_{eq1} = R_{2a}//R_{2b}//R_{3a}//R_{3b} \tag{2.12}$$

In Fig. 2.6, the gap function block is obtained by the geometrical movement analysis of the motor which is presented in Chapter one.

From the equations of the air gaps, the functions of reluctance of the motor could be obtained from:

$$R_r = l_r/(\mu_r A_r) \tag{2.13}$$

$$R_s = l_s/(\mu_s A_s) \tag{2.14}$$

$$R_1 a = g_{1a}(\Theta)/(\mu_0 A_s) \tag{2.15}$$

$$R_1 b = g_{1b}(\Theta)/(\mu_0 A_s) \tag{2.16}$$

$$R_2 a = g_{2a}(\Theta)/(\mu_0 A_s) \tag{2.17}$$

$$R_2 b = g_{2b}(\Theta)/(\mu_0 A_s) \tag{2.18}$$

$$R_3 a = g_{3a}(\Theta)/(\mu_0 A_s) \tag{2.19}$$

$$R_3 b = g_{3b}(\Theta)/(\mu_0 A_s) \tag{2.20}$$

Where μ_r is the permeability of the rotor, similarly, μ_s is the permeability of the stator, l_r and l_s are the lengths of the flux path in the system. A_r is the surface area of the rotor. And μ_0 is the air permeability which is a constant as it is shown in Fig. 2.6.

Moreover,

$$L_{1a1b} = L_{1a1a} \tag{2.21}$$

Self-inductances of the pole A and mutual inductance between pole A and pole B of the same phase happen to be the same in this case because the flux linkage at tooth 1a is due to the fact that a current that is being generated flows across 1b as well, as it could be seen in Fig. 2.2- 2.3.

Fig. 2.6 is the block diagram representation of self-inductance. The input of the self-inductance block is the numbers of windings, the permeability of the materials, and the electrical speed of the motor.
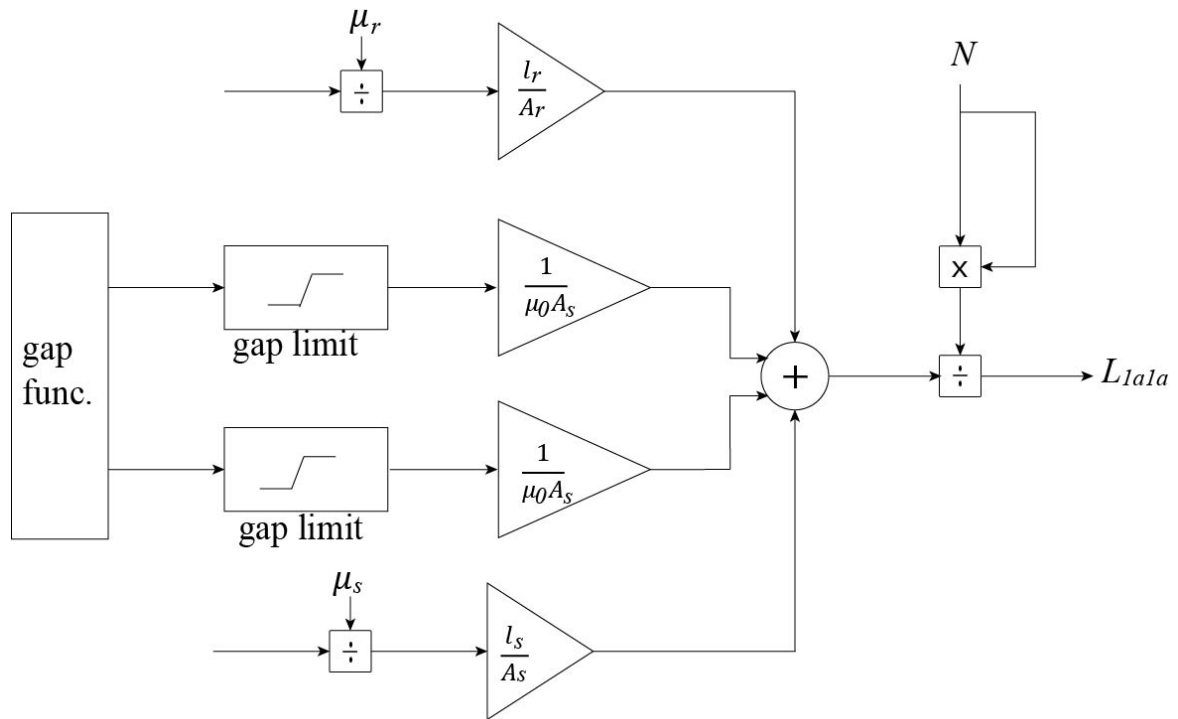
Fig. 2.6. Self-inductance model

And as for mutual-inductances, mutual inductance between poles and the simplified equivalent circuit are shown in Fig. 2.7 and Fig. 2.8.
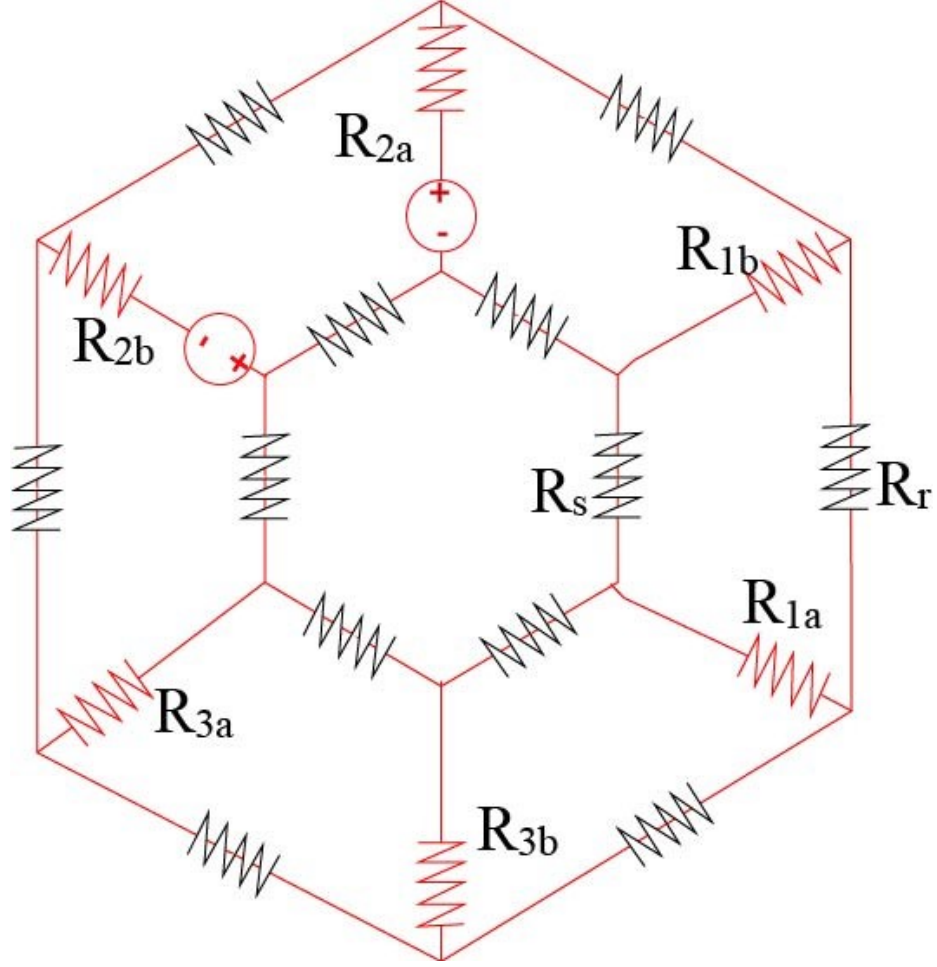
Fig. 2.7. This figure shows the equivalent circuit of the motor to obtain mutual inductance

Moreover, flux linkagees are given by the following equations:

$$\lambda_{1a} = (L_{1a1a} + L_{1a1b})i_1 + (L_{1a2a} + L_{1a2b})i_2 + (L_{1a3a} + L_{1a3b})i_3 \qquad (2.22)$$

$$\lambda_{1b} = (L_{1b1a} + L_{1b1b})i_1 + (L_{1b2a} + L_{1b2b})i_2 + (L_{1b3a} + L_{1b3b})i_3 \qquad (2.23)$$

$$\lambda_{2a} = (L_{2a1a} + L_{2a1b})i_1 + (L_{2a2a} + L_{2a2b})i_2 + (L_{2a3a} + L_{2a3b})i_3 \qquad (2.24)$$

$$\lambda_{2b} = (L_{2b1a} + L_{2b1b})i_1 + (L_{2b2a} + L_{2b2b})i_2 + (L_{2b3a} + L_{2b3b})i_3 \qquad (2.25)$$

$$\lambda_{3a} = (L_{3a1a} + L_{3a1b})i_1 + (L_{3a2a} + L_{3a2b})i_2 + (L_{3a3a} + L_{3a3b})i_3 \qquad (2.26)$$

$$\lambda_{3b} = (L_{3b1a} + L_{3b1b})i_1 + (L_{3b2a} + L_{3b2b})i_2 + (L_{3b3a} + L_{3b3b})i_3 \qquad (2.27)$$
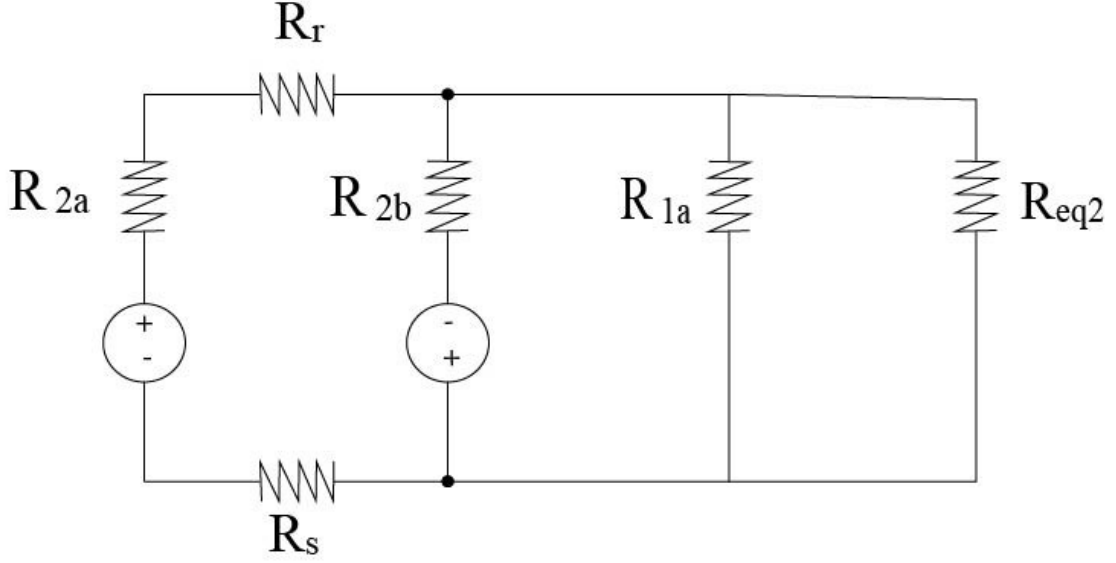
Fig. 2.8. This figure shows the equivalent circuit of the motor to calculate mutual inductance

It is worth to mention that both self-inductance and mutual-inductance are derived assuming that the reluctance over magnetic cores are ignored and for simplification purposes, the effects of the other windings (mutual inductance) are neglected since there will be no overlaps to the voltages applied to the phases initially.

And all the mutual inductances of phase two and phase three can be calculated in similar ways. Similar to the way to obtain self-inductance, mutual-inductance could be obtained by Equ. 2.28.

$$L_{1a2a} = N^2/((R_{2a} + R_{2b} + R_r + R_s)//R_{eq2}//R_{1a}) \tag{2.28}$$

where,

$$R_{eq2} = R_{1b}//R_{3a}//R_{3b} \tag{2.29}$$

For a further simplification, it is assumed that there will be a higher inductance away from the touching point to the ones closer to the contact point. In this case, self-inductance could be obtained by the following:

$$L_{1a1a} = L_{1b1b} = \frac{N^2}{R_{1a} + R_{1b}} = \frac{N^2 \mu_0 A_s}{r_{21}[2 - \sqrt{3}\cos(\theta)]} \tag{2.30}$$

$$L_{2a2a} = L_{2b2b} = \frac{N^2}{R_{2a} + R_{2b}} = \frac{N^2 \mu_0 A_s}{r_{21}[2 - \sqrt{3}\cos(\theta - 2\pi/3)]} \tag{2.31}$$

$$L_{3a3a} = L_{3b3b} = \frac{N^2}{R_{3a} + R_{3b}} = \frac{N^2 \mu_0 A_s}{r_{21}[2 - \sqrt{3}\cos(\theta + 2\pi/3)]} \tag{2.32}$$

One thing to note in Fig. 2.6 is that a limit of the gap function is important in the simulation since the reluctance is the reciprocal coefficient of the gap, which means reluctance will go to infinity unless it is limited. For this reason, a special gap limit symbols is used in this block shown in Fig. 2.6.

2.3 Block Diagram Representation to Obtain Phase Torque

Since it is a three-phase electric motor, the electric torque of each phase is referred as phase torque in this thesis.

As for the energy, the total energy of the system and electromagnetic torque could be obtained respectively from the following equations:

$$W_c = (L_{1a1a} + L_{1b1b})i_1^2 + (L_{2a2a} + L_{2b2b})i_2^2 + (L_{3a3a} + L_{3b3b})i_3^2 \tag{2.33}$$

$$T_e = \frac{dW_c}{d\theta} = \triangle T_1 + \triangle T_2 + \triangle T_3 \tag{2.34}$$

And since $L_{1a1a} = L_{1b1b}$, therefore, in Fig. 2.9, phase torque is defined by the self-inductance and phase currents of the motor, which is obtained from:

$$\triangle T_1 = 2\frac{dL_{1a1a}}{d\theta}i_a^2 \tag{2.35}$$

$$\triangle T_2 = 2\frac{dL_{2a2a}}{d\theta}i_b^2 \tag{2.36}$$

$$\triangle T_3 = 2\frac{dL_{3a3a}}{d\theta}i_c^2 \tag{2.37}$$
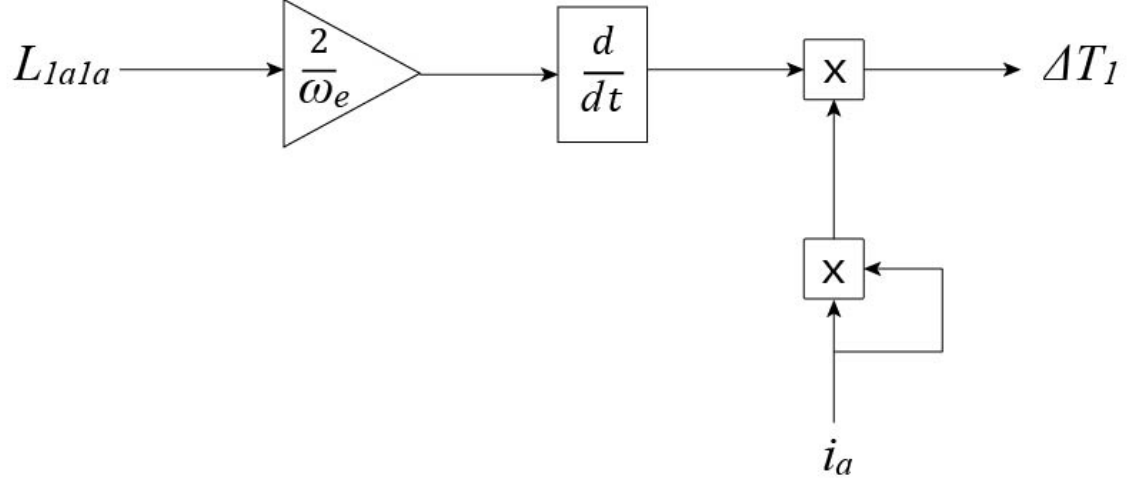
Fig. 2.9. Phase torque model

According to Equ. 2.20 to Equ. 2.23, phase torques could be obtained by:

$$\triangle T_1 = -\frac{2\sqrt{3}r_{21}\sin\theta N^2\mu_0 A_s}{(2r_{21} - r_{21}\sqrt{3}\cos(\theta))^2}i_a^2 \tag{2.38}$$

$$\triangle T_2 = -\frac{2\sqrt{3}r_{21}\sin(\theta - 2\pi/3)N^2\mu_0 A_s}{(2r_{21} - r_{21}\sqrt{3}\cos(\theta - 2\pi/3))^2}i_b^2 \tag{2.39}$$

$$\triangle T_1 = -\frac{2\sqrt{3}r_{21}\sin(\theta + 2\pi/3)N^2\mu_0 A_s}{(2r_{21} - r_{21}\sqrt{3}\cos(\theta + 2\pi/3))^2}i_c^2 \tag{2.40}$$

Only one phase (phase one) is shown in this block diagram (Fig. 2.9), whereas the other two phases are done in a similar matter.

2.4 Block Diagram Representation to Obtain Mechanical Speed

Fig. 2.13 shows the electrical torque which is dependent on $\triangle T1, \triangle T2$, and $\triangle T3$ as well as the load torque T_{load} applied to the system.

And,

$$T_e = \triangle T_1 + \triangle T_2 + \triangle T_3 \tag{2.41}$$

Then the mechanical speed could also be obtained from this block, which is considered as essential as the torque in the real industrial applications. Then, the equation for mechanical speed is written as in Equ. 2.42 (Fig. 2.10):

$$T_e + T_{load} + w_m B_m = J_m \frac{dW_m}{dt} \tag{2.42}$$

In Equ. 2.42, according to Newton's second law, the external torque equals to the angular acceleration times the moment of inertia. Where B_m is the damping coefficient, T_l is the load torque and J_m is the moment of inertia.
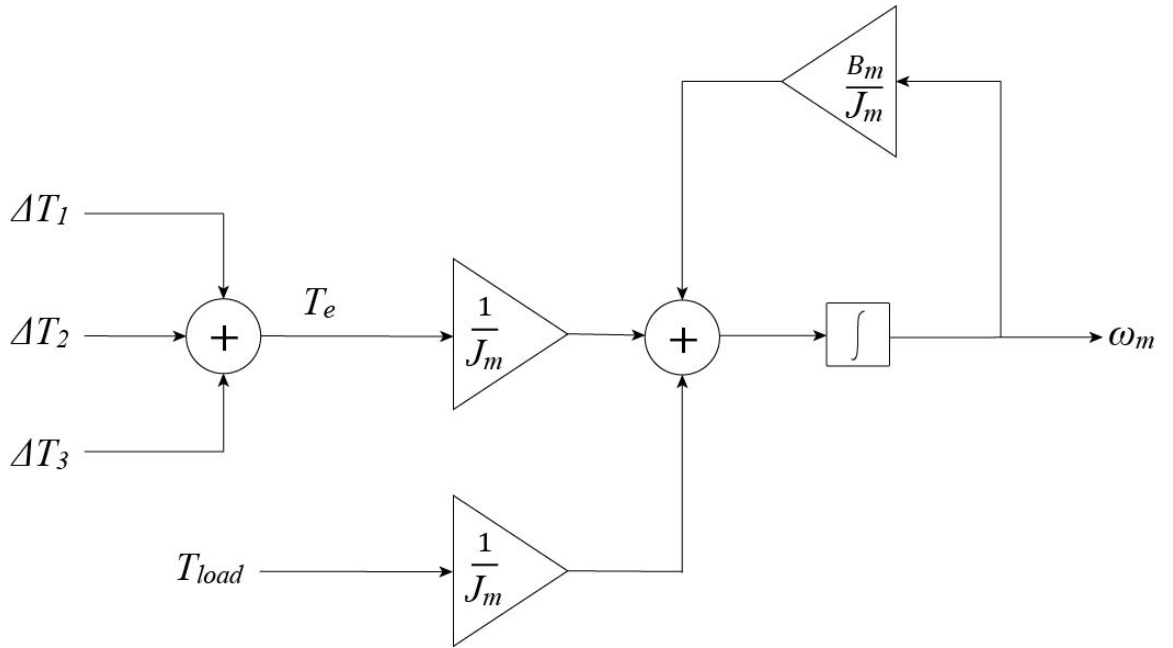
Fig. 2.10. Mechanical speed model

Moreover, there is another way to find mechanical speed which is shown below:

It is shown in Fig. 2.11, Fig. 2.12 and Fig. 2.13, both center of the rotor and the center of the stator are shown. According to the same figure, the angle α is defined as below:

$$\sin \alpha = AB/r_2 \tag{2.43}$$
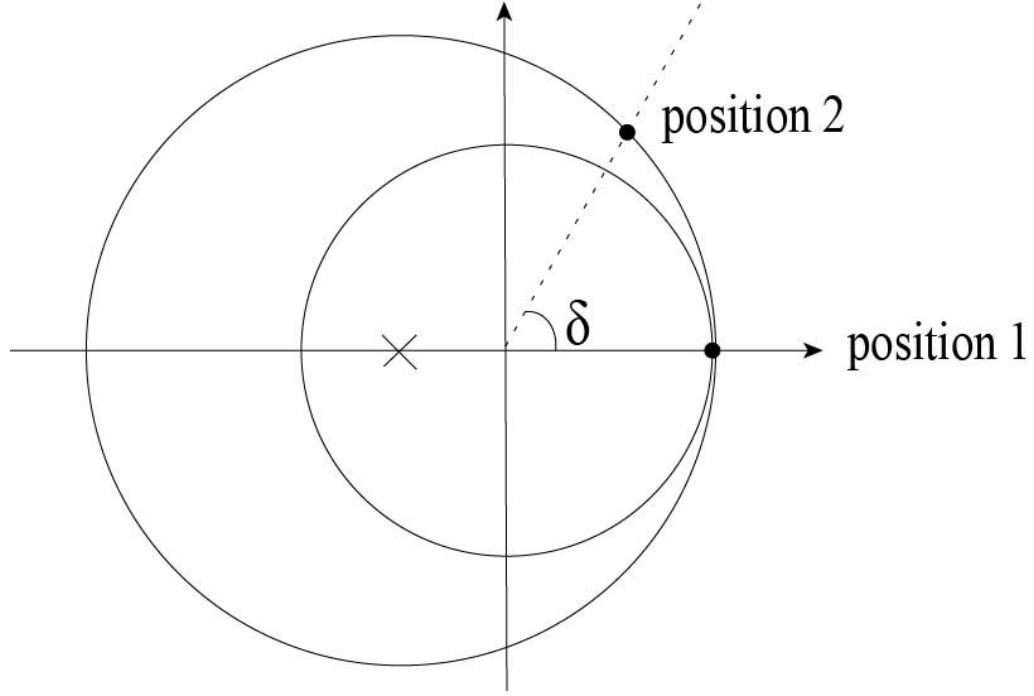
Fig. 2.11. This figure shows the relative positions of the rotor after angle θ

therefore,

$$\alpha = arcsin(AB/r_2) = 2\pi r_{21}/r_2 \tag{2.44}$$

In Fig. 2.12, length X is needed to be found in order to calculate the angle. The angle θ is defined below:

$$X = r_2 \cos \alpha - r_{21} \tag{2.45}$$

$$\theta = \cos^{-1}\left[\frac{r_2 \cos(2\pi r_{21}/r_2) - r_{21}}{r_1}\right] \tag{2.46}$$

And the mechanical speed could be obtained from the following equation:

$$\omega_m = \theta f_e \tag{2.47}$$

$$\omega_m = \frac{\theta}{2\pi}\omega_e \tag{2.48}$$

Where,

$$\theta = \cos^{-1}\left[\frac{r_2 \cos(2\pi r_{21}/r_2) - r_{21}}{r_1}\right]\frac{\omega_e}{2\pi} \tag{2.49}$$
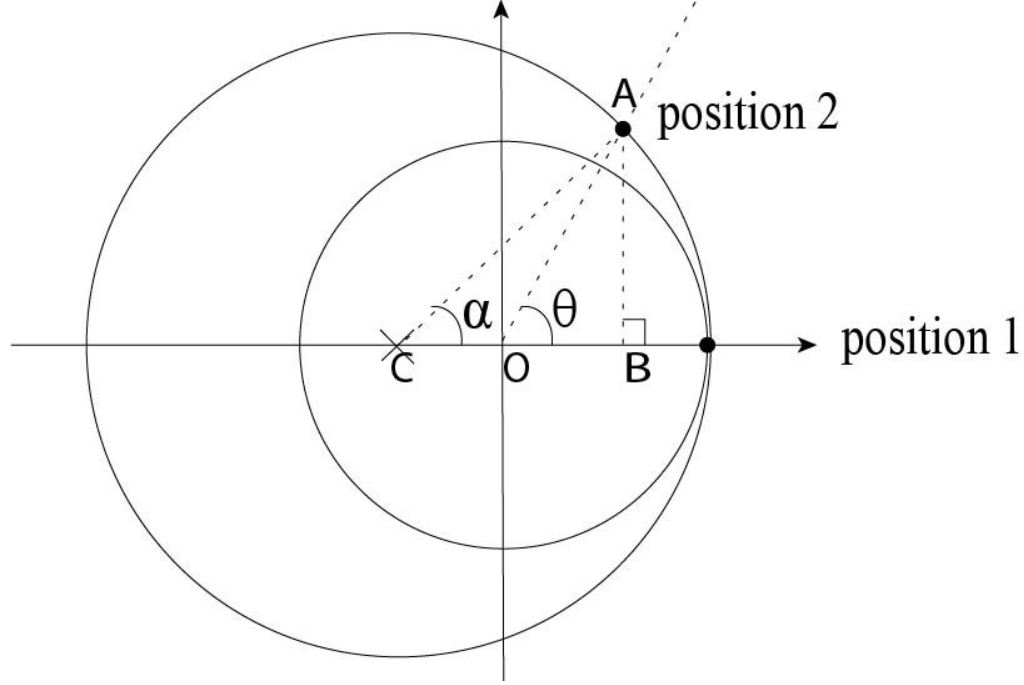
Fig. 2.12. This figure shows the position of the rotor after one electrical period

2.5 Saturation Effect Block Diagram Representation

Because of the permeability factor of the material, machine saturation effect results in vary machine inductances and the assumption of linear magnetic circuits, which standard optimization methods are not suitable [18]. Corresponding magnetization curves (B-H curves or B-μ curves) are used to observe the saturation effects [19] (further discussion is in Chapter three). Therefore adding a saturation block is necessary to emulate a realistic system.

The flux across the core can be written as:

$$\phi = Ni/R \tag{2.50}$$

where i is the phase current, N is the number of the core windings and R is the reluctance of the motor.
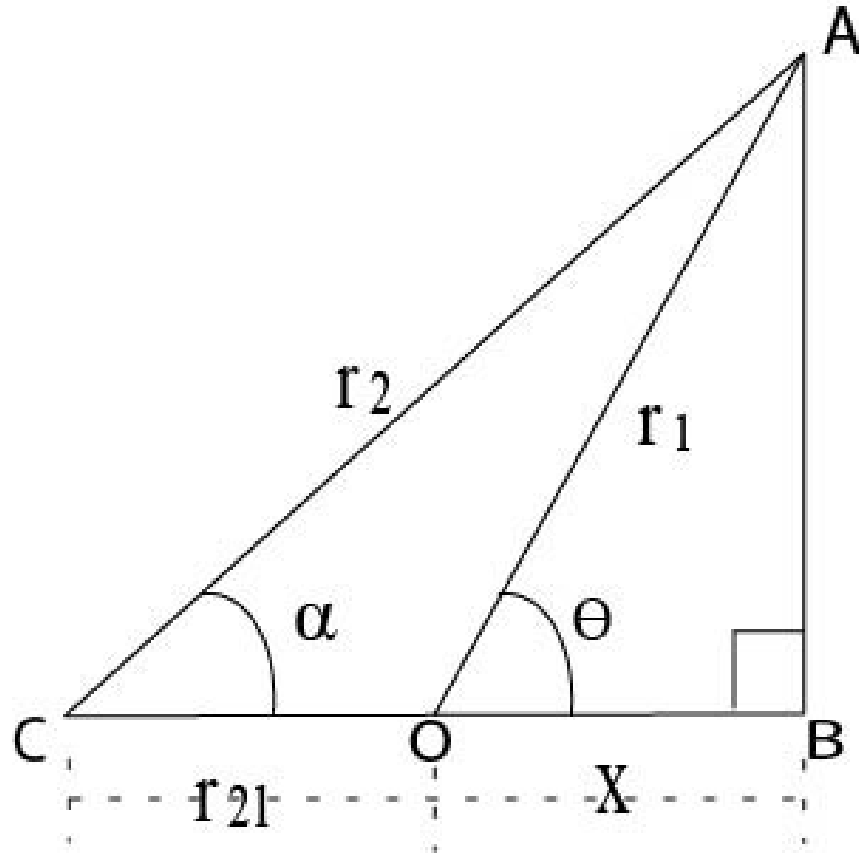
Fig. 2.13. This figure shows the angle between the rotor and stator
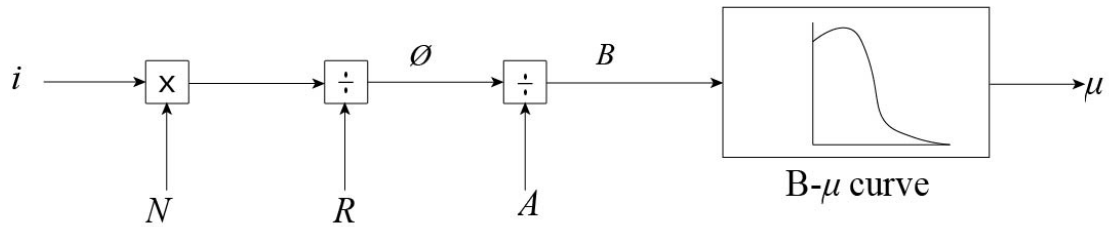
Fig. 2.14. Permeability model with consideration of saturation

This equation above indicates that the magnate flux depends on the number of windings, phase currents and reluctances. Then the magnetic field density in a pole is given by:

$$B = \phi/A \qquad (2.51)$$

The value of B will be as input of a $B-\mu$ look-up table. The look-up table is specified by core materials. Then the look-up table generates an appropriate new value of μ, as shown in Fig. 2.12. This permeability will then be fed back to the system to update the variables in the previous blocks accordingly, such as the self-inductance block, mechanical speed block and phase torque block. This method is called LUT (look-up table) method and is used to deal with saturation effect and a further discussion will be in chapter three of this thesis.

To sum up this chapter, Five SIMULINK simulation block diagrams are presented in this chapter. The first block is the block to obtain the phase currents, the second block is the block to obtain the self-inductance and the third block is the block to obtain phase torque. The last one is the block to obtain the mechanical speed.

Each of these blocks are based on the geometrical configurations of the air-gapless motor, Kirchhoff's Voltage Law (KVL), Ohm's Law, Kirchhoff's Current Law (KCL) and the principle of electromagnetic. Equivalent circuit method is used for the simplification matter.

3. SATURATION EFFECT

3.1 Saturation Effect in Motors and $B - H$ Curve

In the air-gapless motor, an electromagnetic coil will be able to generate magnetic flux. The magnetic flux is usually expressed by the amount of magnetic lines in the specific areas. Therefore, the density of the lines is defined as "Flux Density" with a symbol B. The unit of B is T as in Tesla.

It was proved by [20], compared to the saturation effect, the unsaturated method will produce a higher transient torque, a higher transient current and as for other effects, the rotor speed of the unsaturated model will get to a steady state faster than the rotor speed of the saturated situation.

Flux density could be significantly increased by increasing the currents cross the coils or by increasing the number of turns of the coils. Saturation happens when an increase in the external magnetizing field (H) cannot increase the magnetization of the material further. So when the total magnetic field (B) levels drop off, it appears as non-linear relationships between magnetic field and external magnetizing field [21]. μ is hardly a constant but a function of the field intensity which is defined as below:

$$B = \mu H \tag{3.1}$$

In addition, μ_0 is known as the permeability of air and μ_r is the relative permeabilities of the coil materials. It is worth to note that in this chapter, the permeability μ refers to μ_r versus μ_0.

According to [22], the magnetic $B - H$ characteristic of the cores depend on the up or down shifts on the magnet orientation facing coil axis. Three regulations of the $B - H$ curve are shown as below: 1) when coil axis is placed by north magnetic pole And as it is shown in Fig. 3.1, it is translated to the first quadrant, 2) when coil axis
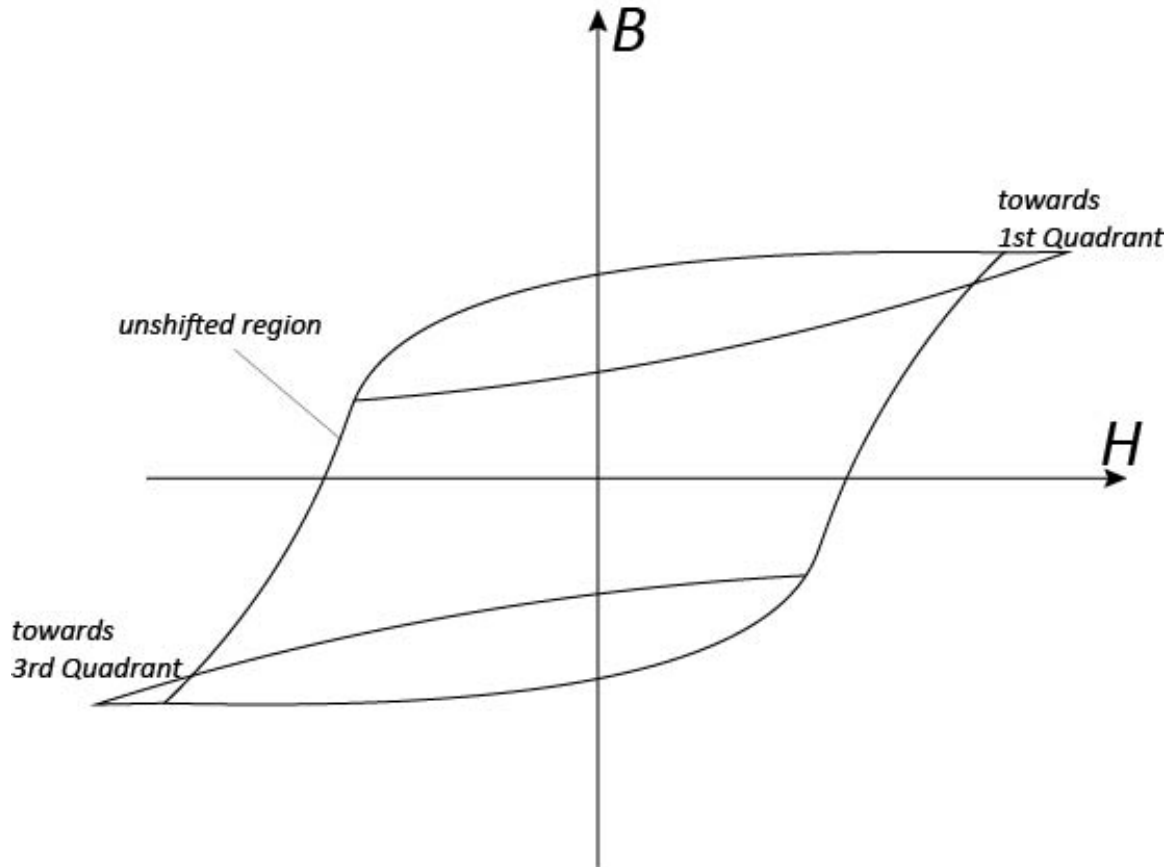
Fig. 3.1. B-H curve of materials

is placed by south magnetic pole And as it is shown in Fig. 3.1, it is translated to the third quadrant and 3) since coil axis and permanent magnet axis are perpendicular to each other so the curve is unsifted.

According to Fig. 3.1, the $B - H$ curve of the materials. In order to reduce the flux density to zero, a reversed current is necessary to use and the reversed current will cause the core to be magnetized in an opposite direction to the direction of the material crystal orientation when it is magnetized in the beginning in which $B - H$ curve moves from the 3rd quadrant to the 1st quadrant. The process is fairly symmetrical which indicates a loop that is called magnetic hysteresis loop.

As for motors and generators, it is important to find a right co-ordinate system for Maxwell's field calculations, subsequently no one system attends both rotor and stator [23]. Once a co-ordinate system is adapted, the process of finding solution of field equations is a rather difficult task, because of the following two reasons: firstly, by the complex figures of the magnetic cores of the rotor and stator and secondly, because of the electrical conductors of the rotor and stator are undefinable [24].

There are studies that have talked about magnetic saturation of motors. 1) The equivalent circuit method (ECM) and numerical analysis (NA) [25] are used in such area. Since NA could take non-linearity of the material property into consideration, it is widely used in researching areas. 2) By using frequency domain instead of time domain to gain a better accuracy when it comes to deal with certain harmonics. This theory is shown in [26]. 3) Applying voltage compensation strategy to reduce the influence of saturation is shown in [27]. 4) To apply 3-D analysis method such as ANSYS to have a view over the relationships between magnetic force and thermal effect [28]. 5) By using on-load and no-load condition [29] to analysis saturation effect happens in electrical motors.

However, in all the years, many researches have been published such as [30] and [31] and saturation is neglected in these papers since the complexity of considering saturation effect due to the following reasons: 1) is able to be complicated by the convergence of iteration calculation, 2) computation time, and 3) computational stability [15], however in [32], though the saturation effect is not neglected, it is only considered up to a limited number of harmonics [33].

Different kind of B-H curves are used to analyze saturation effect. Proposing certain efficient materials from the aspect of gaining a higher torque, less ripple is useful and some ideas are presented in [34] as well as it is discussed in this thesis using SIMULINK simulation.

The conventional unsaturated model could not predict a dynamic behavior of the motor that we applied for the simulation. Especially, since the parameters applied in the SIMULINK system vary, such as the self inductance and the frequency [35],

taking a saturated situation into consideration is more and more crucial to the motor control system. Methods used to simulate the saturation effect are shown in section 3.2.

3.2 The Look-up Table (LUT)

There are two common method to deal with saturation effect, one is 1) applying a look-up table (LUT) and the other one is 2) using Finite element method (FEM).

LUT method costs less efforts and generates the saturation effect intuitively. FEM is a very time consuming method, especially when the phase voltage is generated by an inverter.

As it is shown in Fig. 3.2, by applying LUT method, the tooth flux density is calculated in the Motor Motion Information block according to the SIMULINK simulation models that is mentioned in the previous chapter.

And by applying the look-up table (LUT) of $B - \mu$ curve, the new material permeabilities are obtained from the Saturation Block in Fig. 3.2. It is worth to mention that when applying the look-up table, there are forms of function such as exponential function [36], polynomial function [37] which differ from material to material.

The $B - \mu$ curves are obtained from the data sheets of the certain materials. In this thesis, materials such as carbon steel, soft ferrite, nickel steel and silicon steel are discussed in section three. Then apply these new permeabilities back to the existing Analytical Block. This method is like a feedback of the simulation. The proposed model has been used in MATLAB-SIMULINK environment.

When the input current of the motor increases over the specified limitation [38] and increases the magnetic field density B which is defined by the look-up table, the according permeability of the iron core changes, which also indicates that the self inductance changes accordingly.
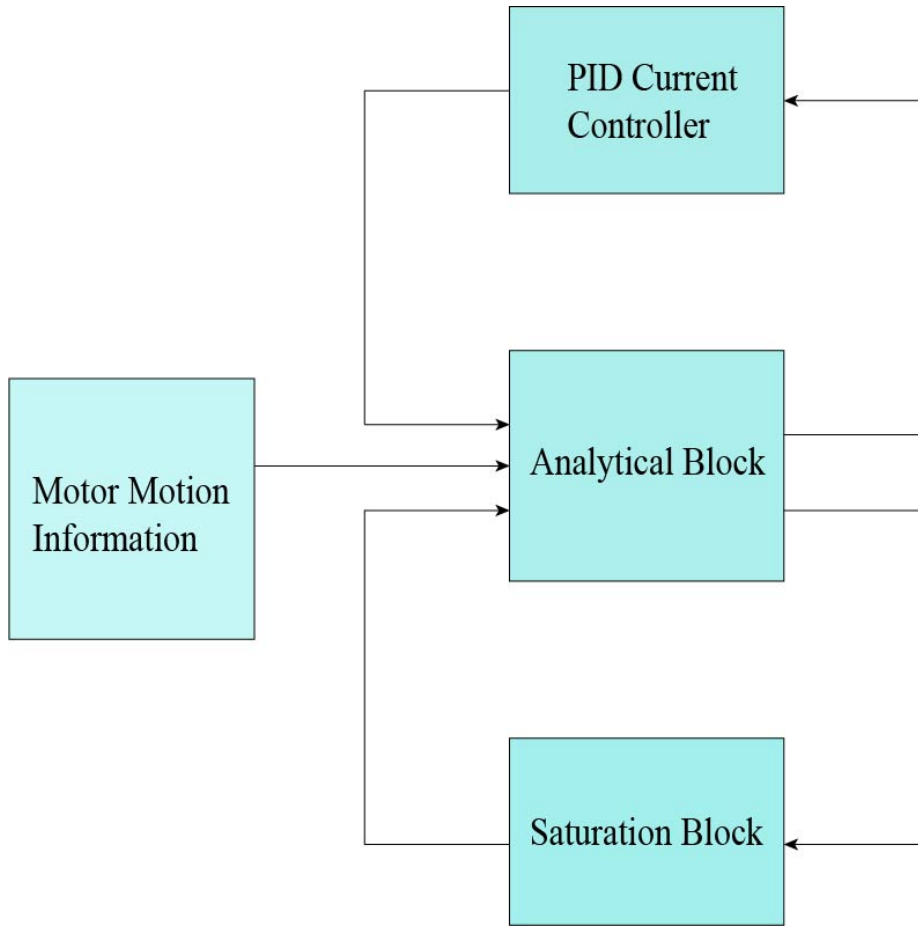
Fig. 3.2. Flow chart including saturation block

3.3 Different $B - \mu$ Curves of Four Different Materials

The magnetic saturation of the iron core depends on three essential conditions [39]: 1) the core materials, 2) the magnetic field currents in the rotor, 3) the stator phase currents and 4) the relative position of the rotor which was mentioned in previous chapter.

As for good ferromagnetic material for electric machines, certain magnetic properties of the magnet materials are considered essential and closely rely on the direction of the quartzes of those materials, the dimensions of the machines, instrumentation for specific ratings, operation efficiency and excitation arrangement.

Here are some related properties to be considered as standards to better magnetic materials: 1) to maintain a rather small loss of eddy current effect therefore obtain a higher electrical resistivity over the voltages, 2) consider to reduce the hysteresis loss and increase the efficiency. It is more desired to have a tapered hysteresis loop or a rather less coercivity [33] 3) a higher temperature capability and 4) having a great energy product [40].

Apparently, there are five different categories of magnetic materials, such as Paramagnetic, Diamagnetic and Ferromagnetic, Antiferromagnetic materials and Ferrimagnetic. Moreover, there are arduous, Soft Magnetic materials and Permanent Magnetic materials. This thesis applies saturation effect to different materials and the upcoming discussion about these materials is in the next section.

3.4   Simulation Results

Behaviors affected by saturation vary from different kinds of materials. They are fairly dependent on the $B - \mu$ curve. For instance, by adding additive materials to the iron metal like nickel could obtain a rather small coercive force, which leads to a smaller hysteresis loop which will change the saturated results. However, having narrow hysteresis loops do not have to appear under the addition of outer material, soft ferromagnetic materials could also cause similar effect.

Applying these kinds of materials are known to generate a higher conduction and obtain an even better conductive behavior, therefore listed as better magnetic materials when it comes to uses of relays, solenoids as well as transformers since they could be magnetized and demagnetized more easily [41].

In addition, the smaller the hysteresis loop, the less the thermal loss of the materials due to the fact that coercive forces are used to conquer the residual magnetism. The residual magnetism will be dissipated through heat. Therefore torque with the saturation effect will have an increased capability and the motor torque stability re-
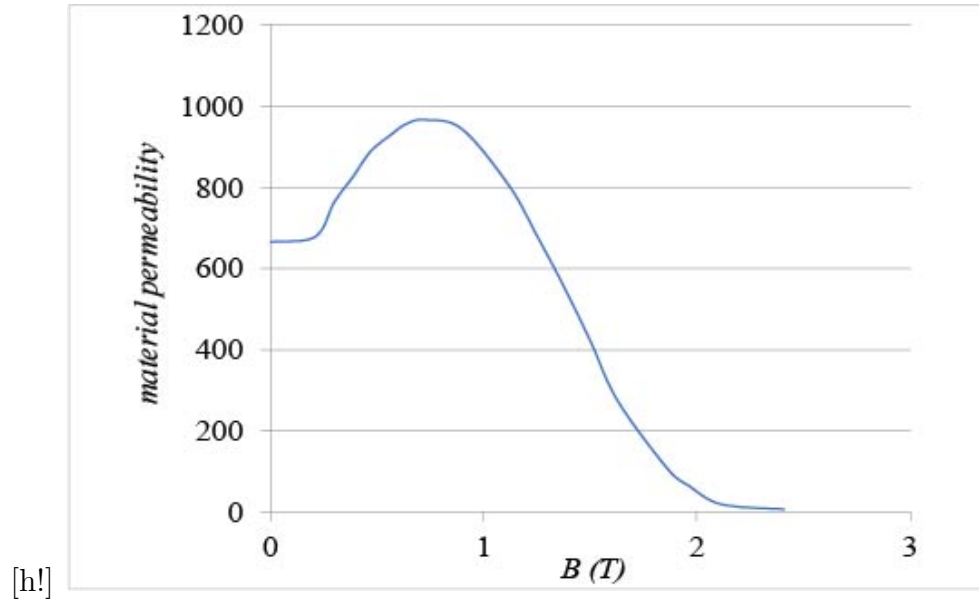
Fig. 3.3. B-μ curve of carbon steels

gion also could be increased. As it is said in [42], the torque stability region could increase at most 21 N.m with different saturation materials.

Also it is noted that the power factor is increased when saturation occurs. This is because the dependency of the motor changes.

3.4.1 Carbon Steel

It is known that carbon steel is a kind of hard magnetic material. Carbon steel is also known as a permanent magnetic material. This material has massive size hysteresis loop and bit by bit rising magnetization curve as it could be seen in Fig. 3.3.

Magnetic flux density of carbon steels is shown in Fig. 3.4. It is obvious that after a certain amount, the curves bend over and become falter on the top, which is an evidence that the saturation occurs. Other permanent materials are tungsten steel, cobalt steel and alnico.
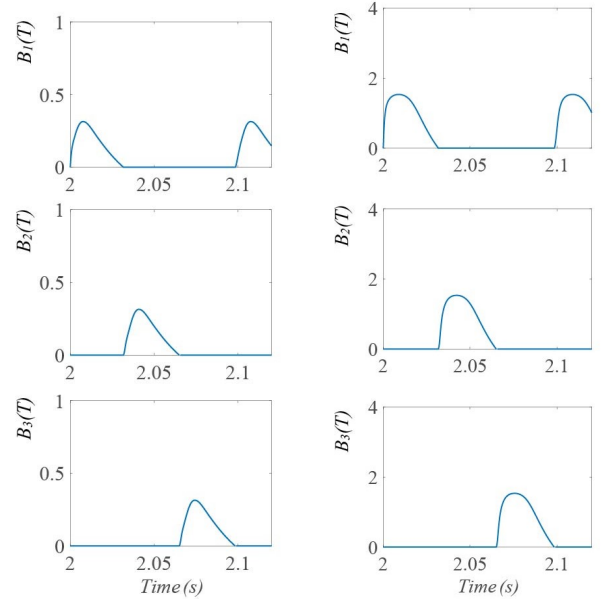
(a) phase current:1A   (b) phase current:6.6A
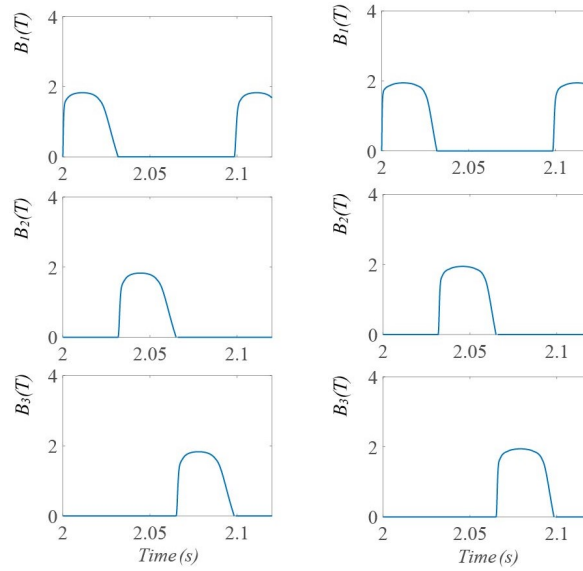
(c) phase current:15A   (d) phase current:25A

Fig. 3.4. Magnetic flux density occurs in carbon steels

3.4.2 Soft Ferrite

Soft ferrite is a kind of soft magnetic materials. Soft magnetic materials are commonly used for the poles of DC machines as well as the rotors of turbo generator.
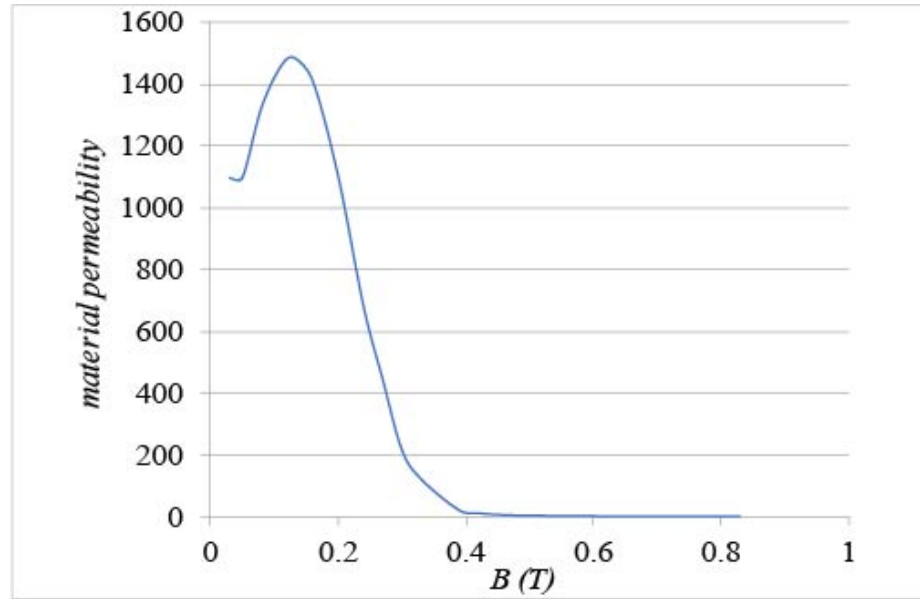
Fig. 3.5. B-μ curve of soft ferrite

Soft ferrite has a tiny size hysteresis loop and a steep magnetization curve. Other soft magnetic materials are forged iron, cast steel, rolled steel and solid steel.

The $B - \mu$ curve is shown in Fig. 3.5. Magnetic field density of soft ferrite is shown in Fig. 3.6, compared to the magnetic field density of the carbon steel, it has a wider retention when the curve reaches to the magnitude. In this case, the saturation effect is more pronounced.

3.4.3   Nickel Steel

Nickel iron alloy has higher permeability and the addition of chromium ends up making it as a better magnetic material. The $B - \mu$ curve of nickel iron is shown in Fig. 3.7. the size of hysteresis loop of nickel iron is very narrow compared to both carbon steels and soft ferrite, which means nickel iron has a better magnetized behavior and it is list as a better magnetic material. Moreover, the curve of nickel iron could reach to a high permeability within in a small amount of time.

(a) phase current:1A   (b) phase current:6.6A

(c) phase current:15A   (d) phase current:25A

Fig. 3.6. Magnetic flux density occurs in soft ferrite

The magnetic field density of nickel steel is shown in Fig. 3.8. In general, it has two characteristic: 1) higher average magnitude and 2) it shows a rather rapid change which leads to a larger slope compared to both carbon steel and soft ferrite.
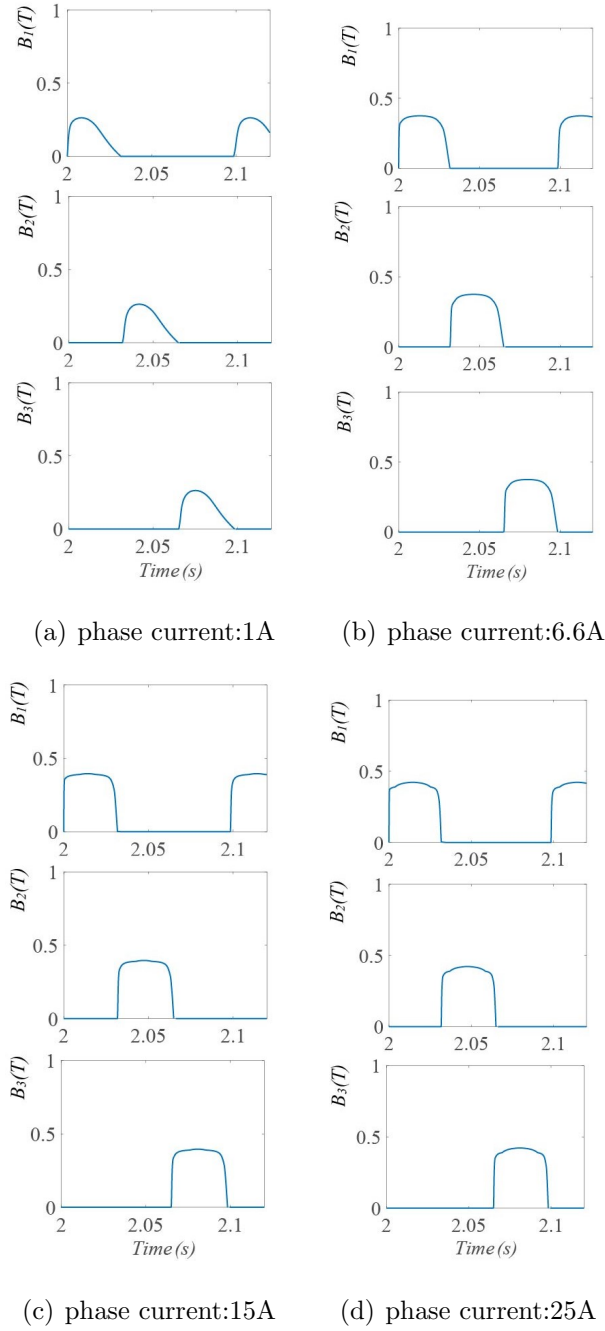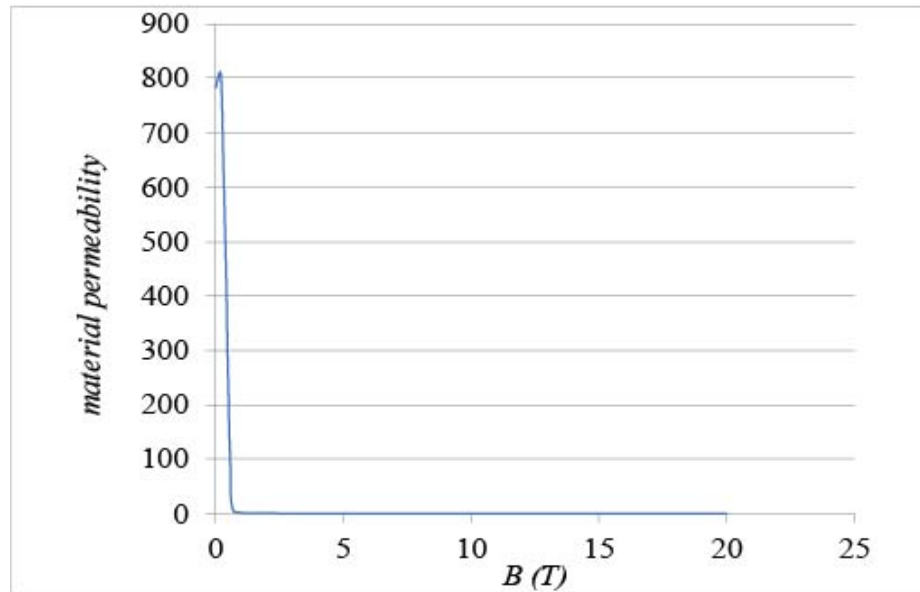
Fig. 3.7. B-μ curve of nickel steels

3.4.4   Silicon Steel

Silicon steel is a mix type of a approximately 0.3 percent of iron and a 4.5 percent of silicon. The idea is to reduce the aging of the materials and cut back the core loss by adding a small amount of silicon. Small silicon contented steels or dynamo grade steel is commonly applied in electric motors. Silicon steel generates higher flux density.

In fact, a great contented silicon steel with more percentage of silicon is applied in transformers. It is shown in Fig. 3.9 that silicon steel also has a rather rapid growth when B is 0 and it reaches to almost 6000 in a very small amount of time which indicates that silicon steel could also be used as a good magnetic core material.

However, the $B - \mu$ curve of silicon steel stays longer as B increases compared to nickel steel. In this case, it might not be as competitive as nickel steel. $B - \mu$ curve of nickel steel is shown in Fig. 3.9 and the magnetic flux density under different currents are shown in Fig. 3.10. It is seen in Fig. 3.10, silicon steel gives a higher magnetic field density. This is because silicon steel has a wider hysteresis loop.
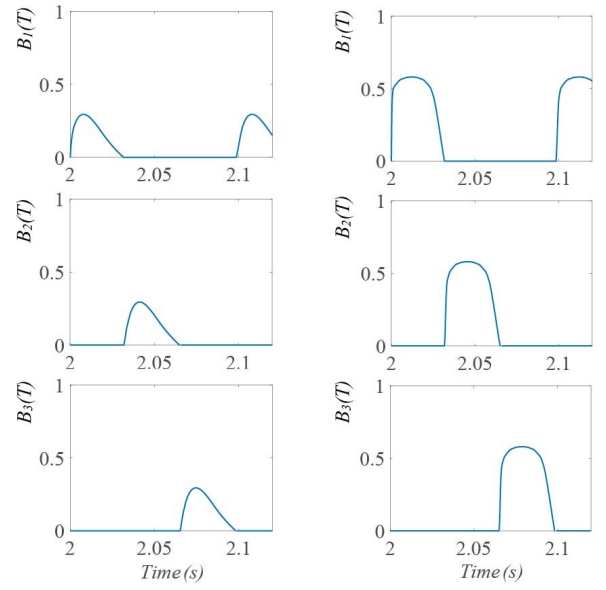
(a) phase current:1A   (b) phase current:6.6A
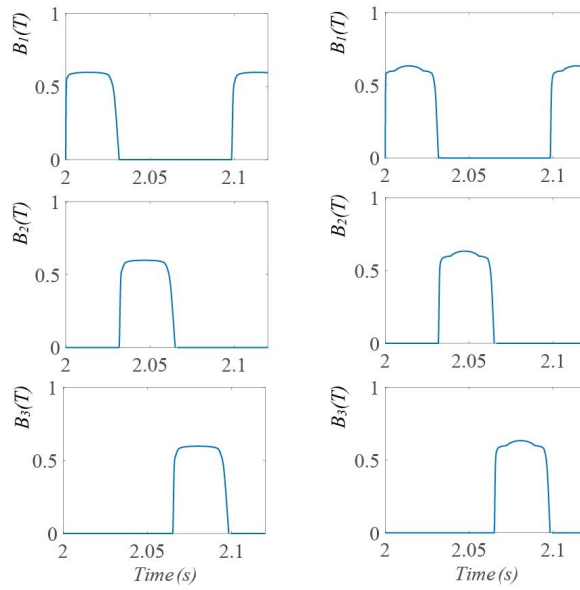
(c) phase current:15A   (d) phase current:25A

Fig. 3.8. Magnetic flux density occurs in nickel steels

Two methods are applied to start the analysis of these electric torques. The first one is to compare the torques under the same current conditions. The second method is to compare the torques among four different materials.
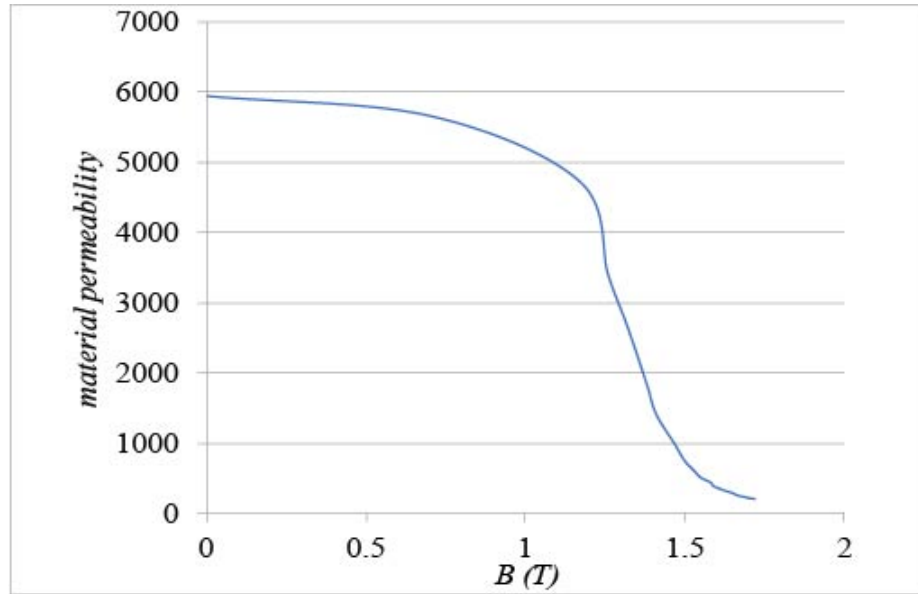
Fig. 3.9. B-μ curve of silicon steels

As it is shown in Fig. 3.11 - Fig. 3.14, there are four levels of currents applied to the system and it is obvious that the more the currents which are injected to the coil, the higher the magnitudes of the torques.

Along with the increase of the currents cross the coil, the torque reaches to a certain negative value.

A negative torque is captured because torques are derivatives of self-inductance versus time. Self inductance is the results of N^2 divide by the total reluctance. Reluctance in the saturated situation is the sum of the reluctance which is caused by the gap function as shown in the previous chapter and the reluctance that is caused by the new μ. The component with the new material permeability μ is a real variable which come from the LUT (the Look-up table of different materials).

The derivative of the self-inductance not only depends on the gap function but also depends on the dynamic $B - \mu$ curve. It could be observed that different materials tend to show a different tolerance level of the negative torques.

For instance, both carbon steel and silicon steel only have negative torques when the magnitudes of the phase currents are greater than 6.6A. On the other hand, both

(a) phase current:1A   (b) phase current:6.6A

(c) phase current:15A   (d) phase current:25A
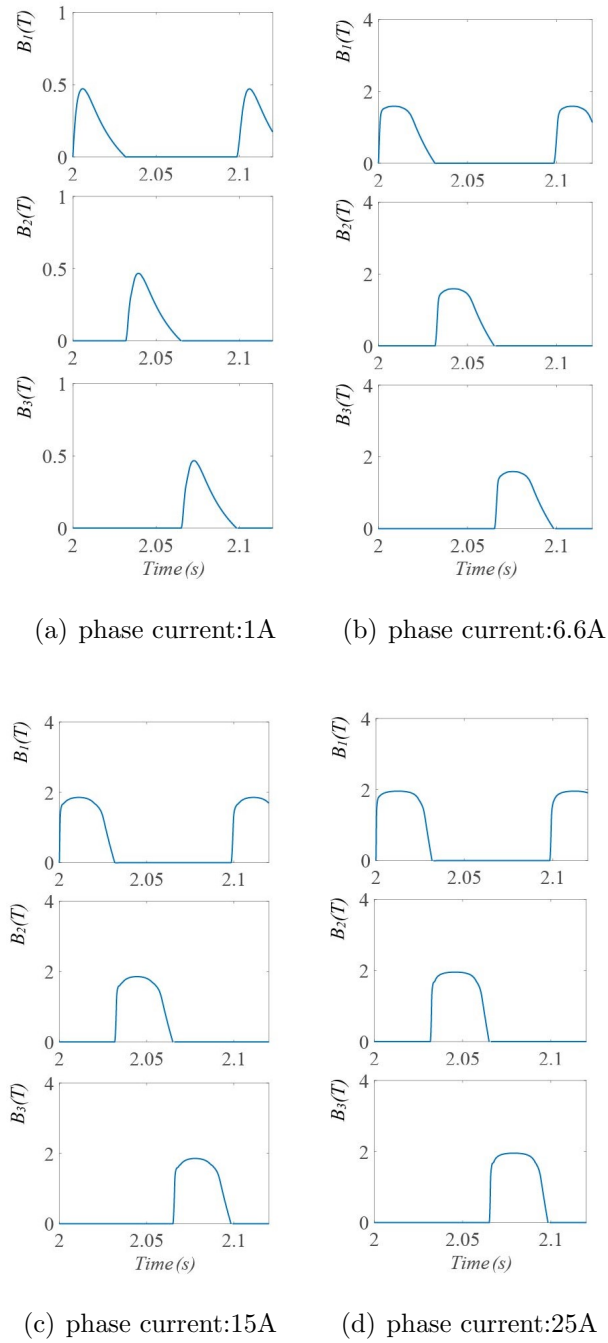
Fig. 3.10. Magnetic flux density occurs in silicon steels

soft ferrite and nickel steel appear a lower tolerance since they tend to have negative torques when the magnitude of the phase currents are greater than 1A.

(a) phase current:1A

(b) phase current:6.6A

(c) phase current:15A

(d) phase current:25A
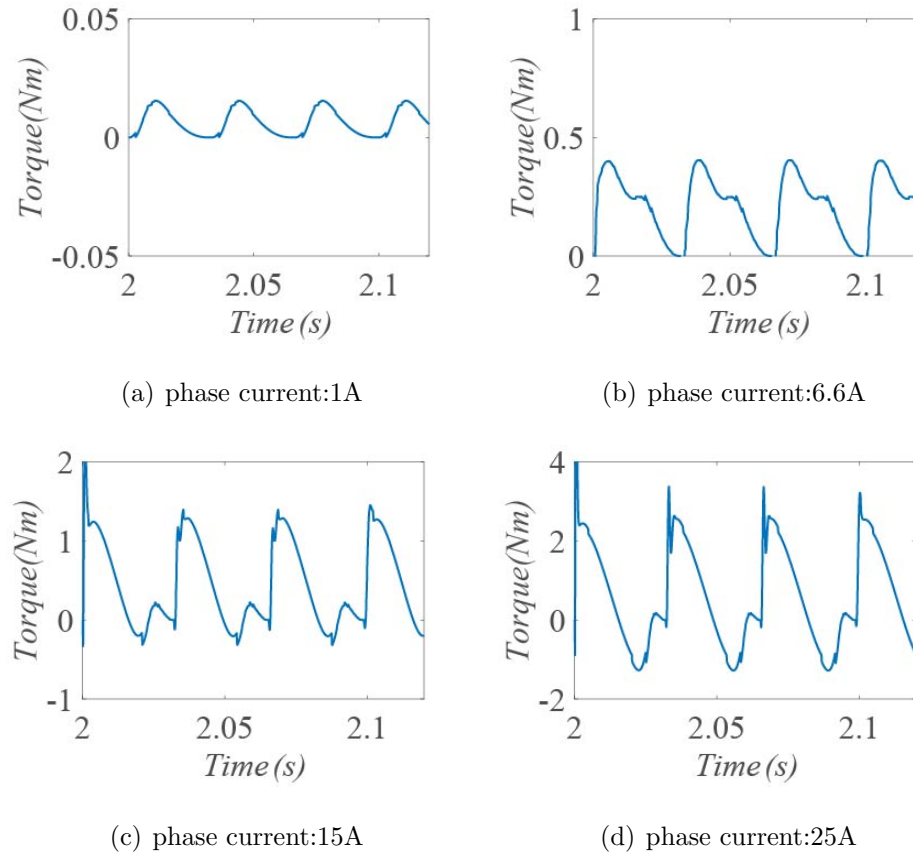
Fig. 3.11. Torque of carbon steels

In this case, if torques are required to be positive all the time, it would be essential to take a look at the actual materials which are used in the system because after the saturation happens in application, this factor would be able to affect the results, which is why saturation should be take into consideration in any further discussions in the motor modeling methods.

Moreover, comparing to nickel and soft ferrite materials, carbon steel and silicon steel actually generate higher torques. So even they are not as conductive as soft ferrite or nickel steel, in the case of torque generations, they give higher torques than nickel steel and soft ferrite. The characteristics of these four materials are presented in the Table 3.1. Table 3.1 shows three characteristics with phase currents at 6.6A. It describes the characteristics of the $B - \mu$ curves of these four materials. Carbon

Table 3.1.
Characteristics of the Materials with saturation

Material	$B - \mu$ curve	B (T)	Torque (N.m)
Carbon steel	wide hysteresis loop	1.80	0.45
Soft ferrite	narrow hysteresis loop	0.45	0.10
Nickel steel	narrow hysteresis loop	0.51	0.20
Silicon steel	wide hysteresis loop	1.90	0.62

(a) phase current:1A

(b) phase current:6.6A

(c) phase current:15A

(d) phase current:25A
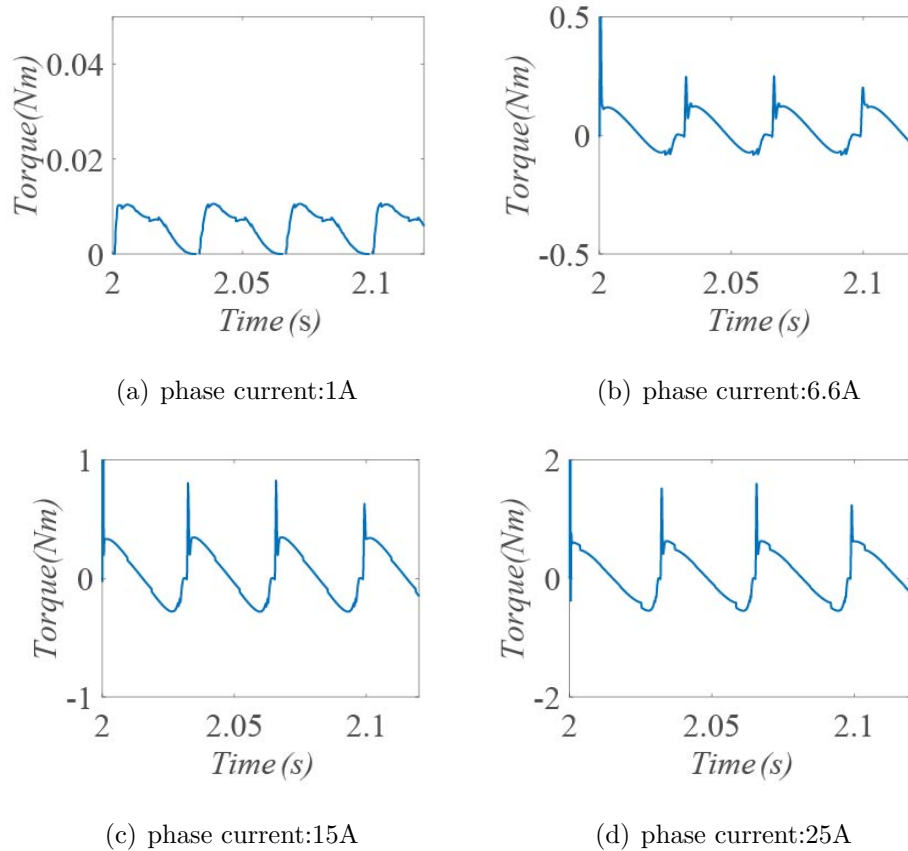
Fig. 3.12. Torque of soft ferrite

steel and silicon steel have wider hysteresis loops compared to soft ferrite and nickel steel. Wider hysteresis loops usually give larger torque stability regions. Thus in the third column, both carbon steel have higher torques.

To sum up this chapter, by applying the SIMULINK simulation blocks that are mentioned in Chapter two, magnetic field densities of the four different materials are obtained. Applying a look-up table is an efficient method to deal with the saturation situation in the motor. Magnetic field density is used as input of the look-up table and the output of it is the new material permeability. This material permeability is then applied to the Analytical Block of the motor which is shown in Fig. 3.2. Therefore, variables in the Analytical Block are changed accordingly, such as phase currents, self-inductance and eventually the torques.

(a) phase current:1A

(b) phase current:6.6A

(c) phase current:15A

(d) phase current:25A
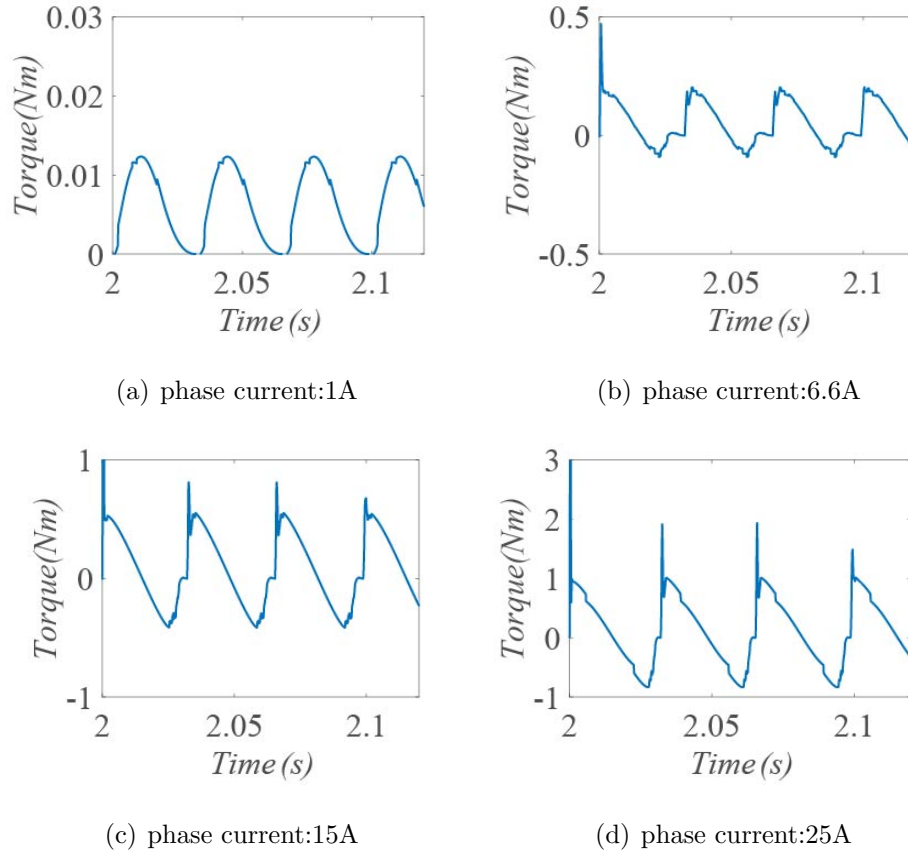
Fig. 3.13. Torque of nickel steels

This chapter compares four different saturated materials which are applied to an air-gapless motor to observe how the torque would be affected. The materials presented are carbon steel, soft ferrite, nickel steel and silicon steel. From Table. 3.1, both silicon steel and Carbon steel generate higher electrical torques. Although silicon steel is more expensive than these other materials, it reveals a critical discussion in the field. This cost plays an important role on why carbon steel is used widely in industry.

(a) phase current:1A

(b) phase current:6.6A

(c) phase current:15A

(d) phase current:25A
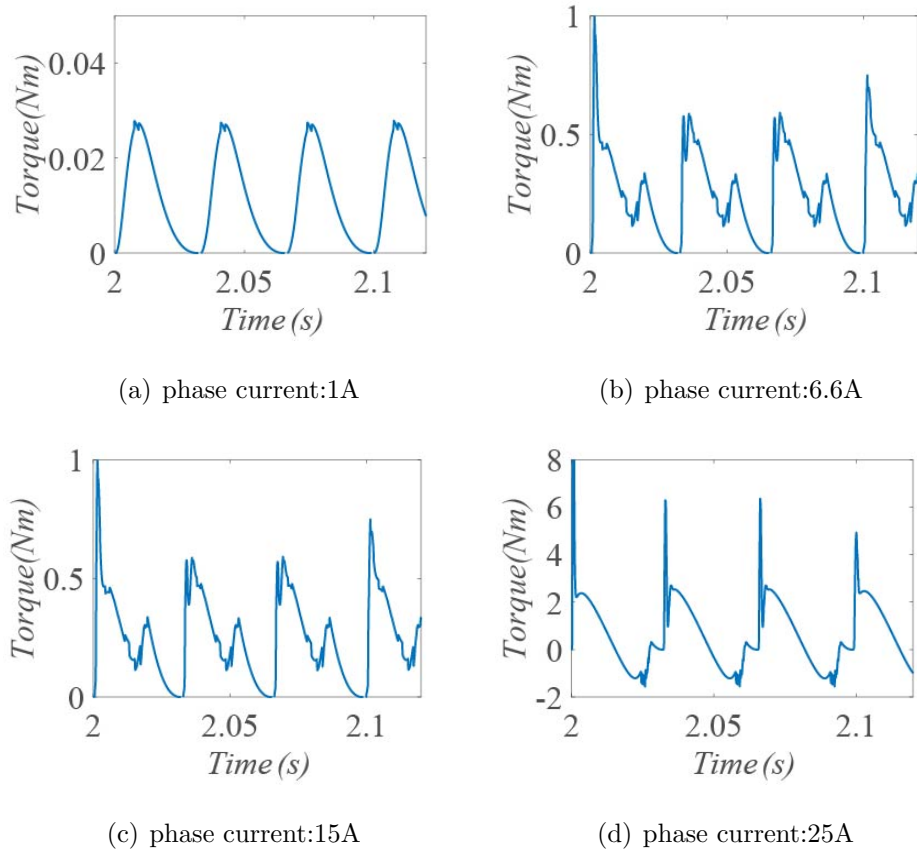
Fig. 3.14. Torque of silicon steels

4. CURRENT CONTROLLER

In this chapter, firstly, a three-phase inverter is proposed to the system and the intriguing gate signals are generated by the Pulse Width Modulation (PWM). Secondly, a ProportionalIntegralDerivative (PID) current controller is presented in this chapter to generate rectified phase currents of the motor. And PID tuning methods are discussed in the end of this section.
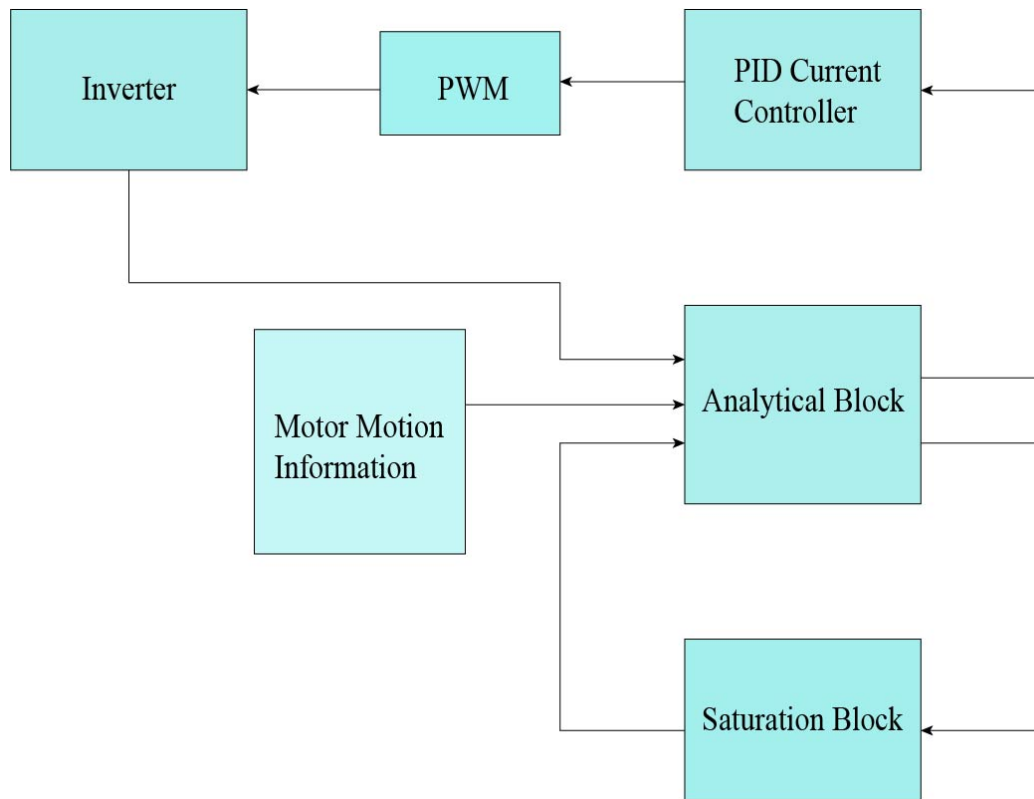
Fig. 4.1. flow chart of the system with the inverter

In Fig. 4.1, A flow chart of the system is shown with the PWM block and the inverter block. So phase currents are measured in the analytical block and are sent to the PID controller block. In the PID controller block (Fig. 4.2), three-phase

rectified reference currents are provided to the system in order to control the currents in specific shapes.
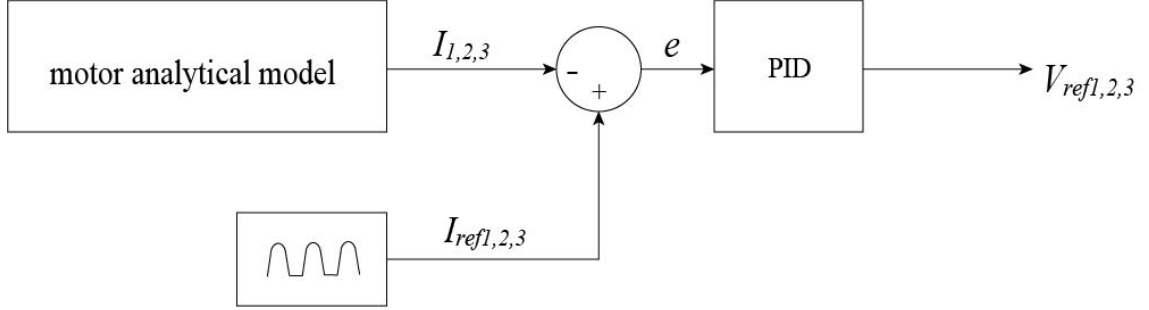
Fig. 4.2. H-bridge inverter configuration

The reason of using rectified currents instead of using square waveforms as the reference currents of the PID controller as most other studies do [43] is because rectified currents are much more realistic than square waveforms in real applications. In real applications, rapid changes in the square waveforms do not exist. These rectified signals are then given to the comparator of the PWM block (Fig. 4.4) along with the triangle waveforms to generate gate signals to the inverter. Moreover, the accuracy of the inverter increases as the frequency of the triangle waveform increases.

After the inverter, actual voltages are captured at the end of each phase and then are injected to the analytical block again as a main feedback of the simulation.

4.1 Three-phase H-bridge Inverter

4.1.1 Advantages of H-bridge Inverter

PWM motivated inverters are widely used in the industry and the configuration is shown in Fig. 4.3. Inverters with the PWM modeling strategy provides better results especially when the frequency are increased.

There are majority of drive manufactures and many topologies related to voltage-source converters, for instance, 1) three-level neutral-point clamped converter, 2) cascaded H-bridge converters and 3) four-level flying capacitor converter. Different kind of topologies generate different levels of voltage of each phase. However, H-bridge inverters are usually being considered as most efficient ones [44].

Here are two main advantages of PWM controlled H-bridge inverter: 1) very efficient: PWN controlled H-bridge inverter has distortion higher than linear amplifier, but a linear amplifier has, 50 percent efficiency at most 2) very commonly used for motor drives where voltage and frequency control are needed.
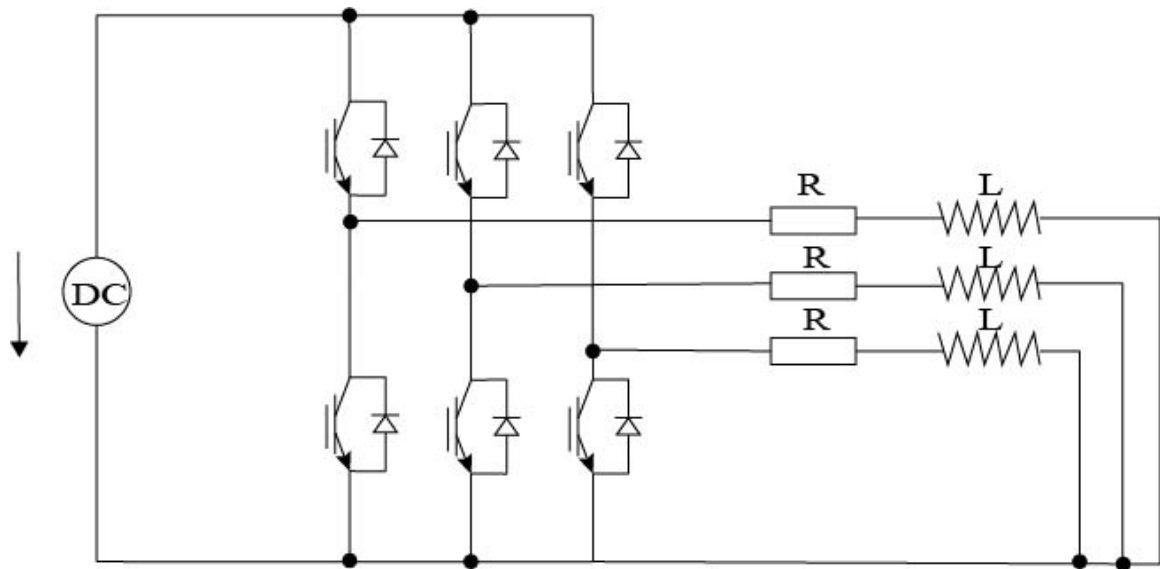
Fig. 4.3. H-bridge inverter configuration

Faults in the inverter often happen and depend on the level of inverters, which may leads to dis-functions of certain mechanical parts. Meanwhile, aging of the mechanical parts as well as total deterioration could be found along these faults, which differ from method to method. Faults could also cause high inertia and vibrations. Such faults are: 1) high impedance type failure of a single IGBT switch, 2) low impedance type failure of a single IGBT switch and 3) asymmetric cross-faults [45].

For example, after the rectified phase currents being injected to the model, there are some expected spikes coming along with the signals, as seen in Fig. 4.7. The spikes could be avoided using a second order low pass filter by getting rid of the certain harmonics. Many studies have been dedicated in this field [46] [47] [48] regarding to the power loss in the inverter.

4.1.2   Gate Signals of H-bridge Inverters

The inverter has eight switch states in order to make the circuit satisfy the KVL and the KCL, both of the switches in the same leg cannot be turned on at the same time due to the fact that it would short the voltage source. Thus the behaviors of the two switches from the same leg are complementary. In Fig. 4.4, this block diagram is used to demonstrate how gate signals in the inverter is obtained. There are two signals, one is the phase voltage signal and the other one is the triangle waveform as it is shown in Fig. 4.6, the orange lines are the phase voltage signals and the blue lines are the triangle waveforms. Both of these two signals are injected to the comparator as shown in Fig. 4.4. The signal that is captured from the comparator is one of the gate signal and since switching gate signals are complementary, which is why a NOT gate is applied in Fig. 4.4.
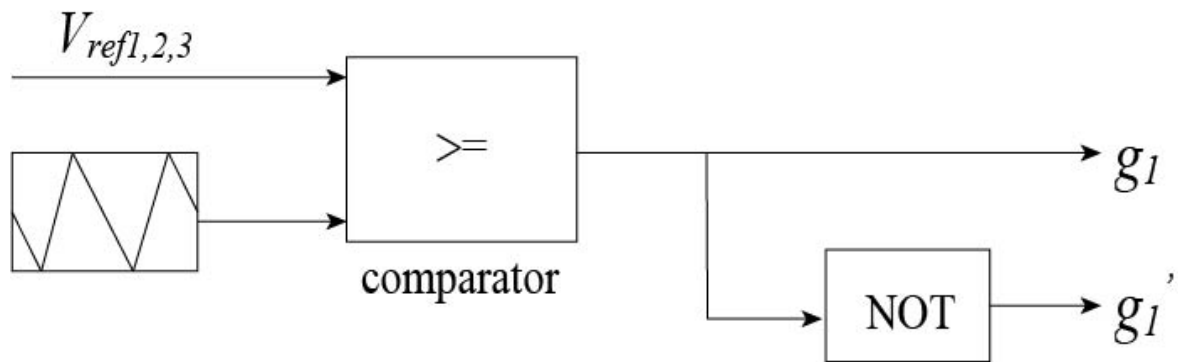
Fig. 4.4. PWM set-up
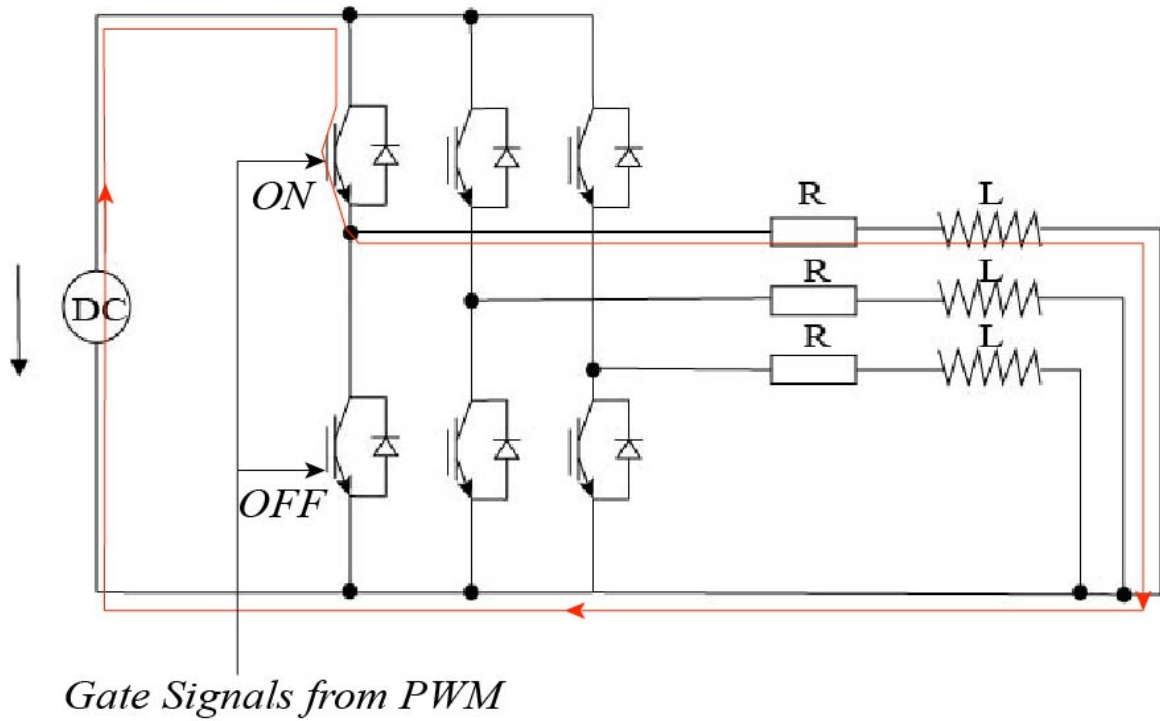
Fig. 4.5. PWM set-up

The gate signals generated from the comparator are shown in Fig. 4.6.

In Fig. 4.7, according to SIMULINK, the data type of the gate signals captured from the comparator are "Double" which means for each phase, both ON and OFF information contain in the same signal. As it is shown in Fig. 4.7, Orange lines depict the ON information and blue lines depict the OFF information. It is worth to mention that OFF information is the ON information after a NOT gate.

(a) phase one   (b) phase two

(c) phase three
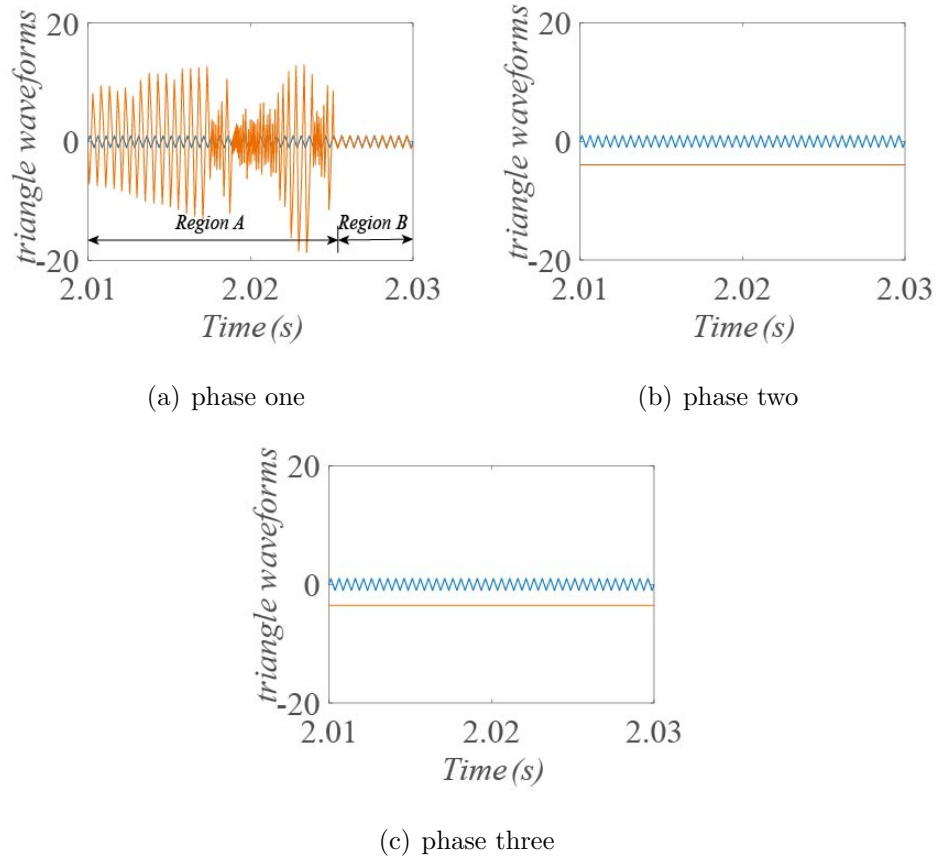
Fig. 4.6. Obtain gate signals for PWM Configuration

4.2 PID Tuning Method

The Proportional-Integral-Derivative (PID) controllers are mostly used in control industry no matter what advantages that other theories, these industries such as heating boilers, stirred-tank plant reactors and batch chemical reactors.

PID controllers are widely used for Multi-Input-Multi-Output (MIMO) systems, Single-Input-Single-Output (SISO) systems [49], stable systems [50] and unstable systems. An example which could be found in [51] is an application of using PID controller for a stable system.

PID controllers simplify systems, comparing to modern control techniques [52], gives a better understanding to control designers. Because of the increased computational power applied in distributed controllers, the needs of selecting PID gains are

(a) phase current:1A

(b) phase current:6.6A

(c) phase current:25A
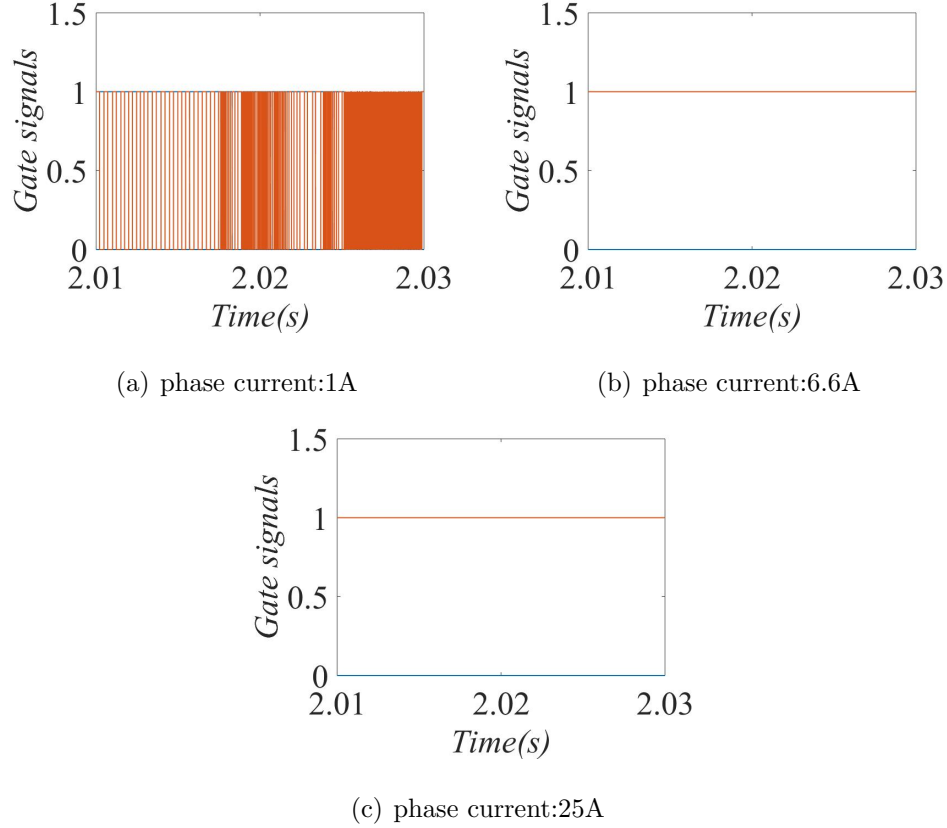
Fig. 4.7. Gate signals of the inverter

more important. Obtaining PID gains is not a easy task since it has to be re-tuned and reconsidered every time in the closed loops which may include adverse conditions and physical damages.

There are four commonly used tuning methods: 1) automatically tuning 2) manually tuning 3) Ziegler-Nichols [53] 4) Cohen-Coon [54]. It was reported in [55], [56] and [57] presents that he particle swarm optimization is used for PID tuning methods with PSO algorithm. Meanwhile Bat Algorithm is proposed by [58], [59] and [60]. As for other algorithms, for instance the Genetic Algorithm [61], Ant System Algorithm [62], and Firely Algorithm [63] have also been proposed. Moreover, certain advantages are obtained from these algorithms, such as 1) increasing rise time, 2) settling time, 3) decreasing overshot as well as 4) steady state error [64].

However among all these methods, Trial and error method is the most commonly used way. Trial and error method takes more time but could obtain more effectiveness that depends on the experience of the person who is tuning it.
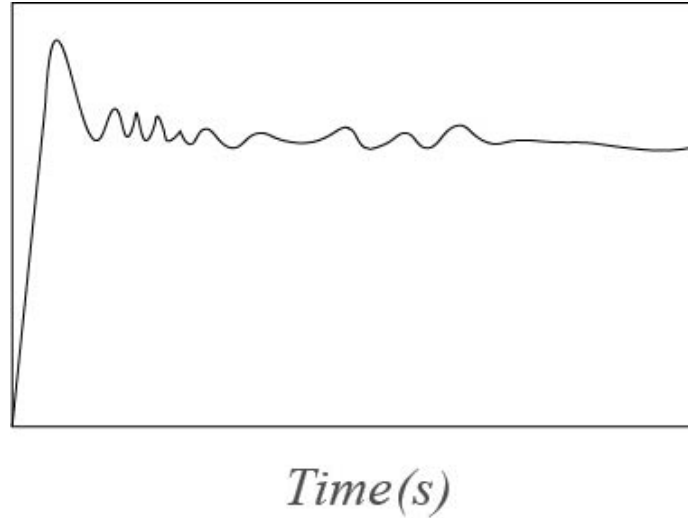
Fig. 4.8. Elements versus Time after the first step

In addition, even for Trial and error method, it is not random but here are some basic steps that could be used for low voltage motors or motors in small dimensions: 1) set all gains to zero. Increase the P gain until the response to a disturbance is close to a steady oscillations as it is shown in Fig. 4.8. 2) Increase the D gain to reduce oscillations 3) Repeat steps 2 and 3 until increasing the D gain does not stop the oscillations. Then set P and D to the last stable values [65].

4.3 Simulation Results

Simulation results of the current controller are presented in this section when the magnitude of the phase currents are 6.5A. In Fig. 4.9, the orange lines in the figure indicate the currents generated by the PID controller and the blue lines represent for the reference currents which are rectified and are injected to the system manually.

(a) current of phase one

(b) current of phase two

(c) current of phase three
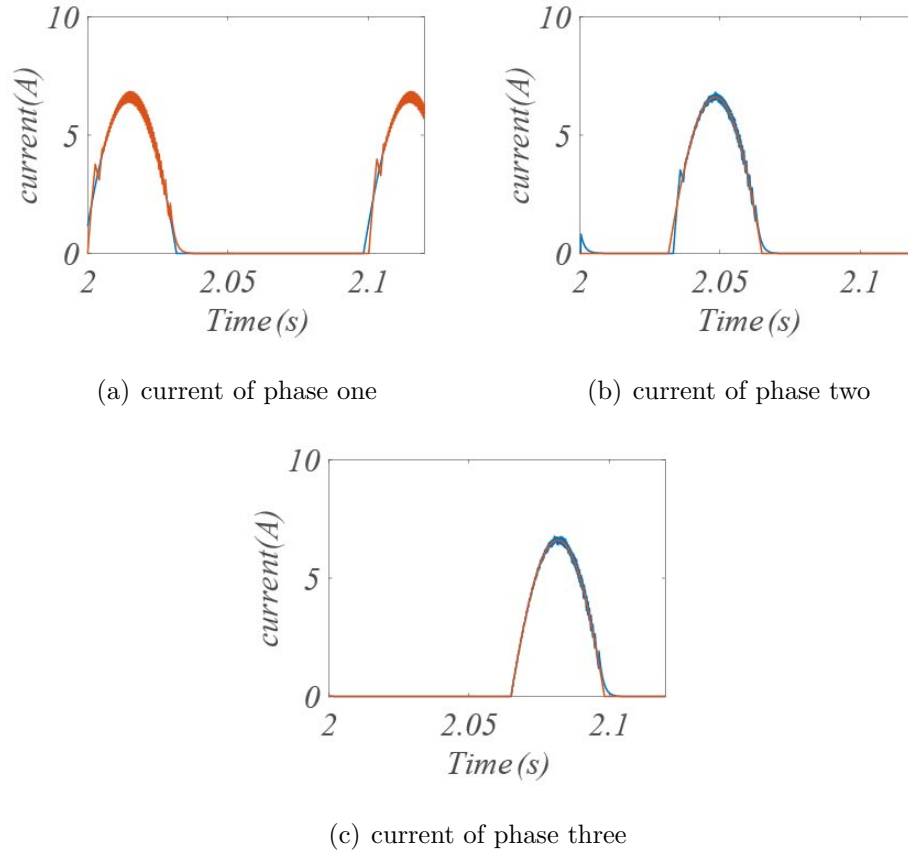
Fig. 4.9. Currents of each phase

As it could be seen in the results, these two kinds of currents are merged accordingly due to the PID controller in Fig. 4.2. It is also worth to mention that choosing gains of the controller could be essential in this case because auto tuning is disabled since the system is non-linear after the inverter and Trail and error method is used in this thesis.

The voltages coming from the ends of the inverter is shown in Fig. 4.10 and the torque is generated in the end which is shown in Fig. 4.11. After applying the inverter, the system remains the same because of the PID current controllers.

The whole SIMULINK block diagram representation is shown in Fig. 4.12. All the block diagram representation s that are mentioned in Chapter two are presented in this figure. It is worth to mention that only one phase of the motor is shown in

(a) voltage of phase one

(b) voltage of phase two

(c) voltage of phase three
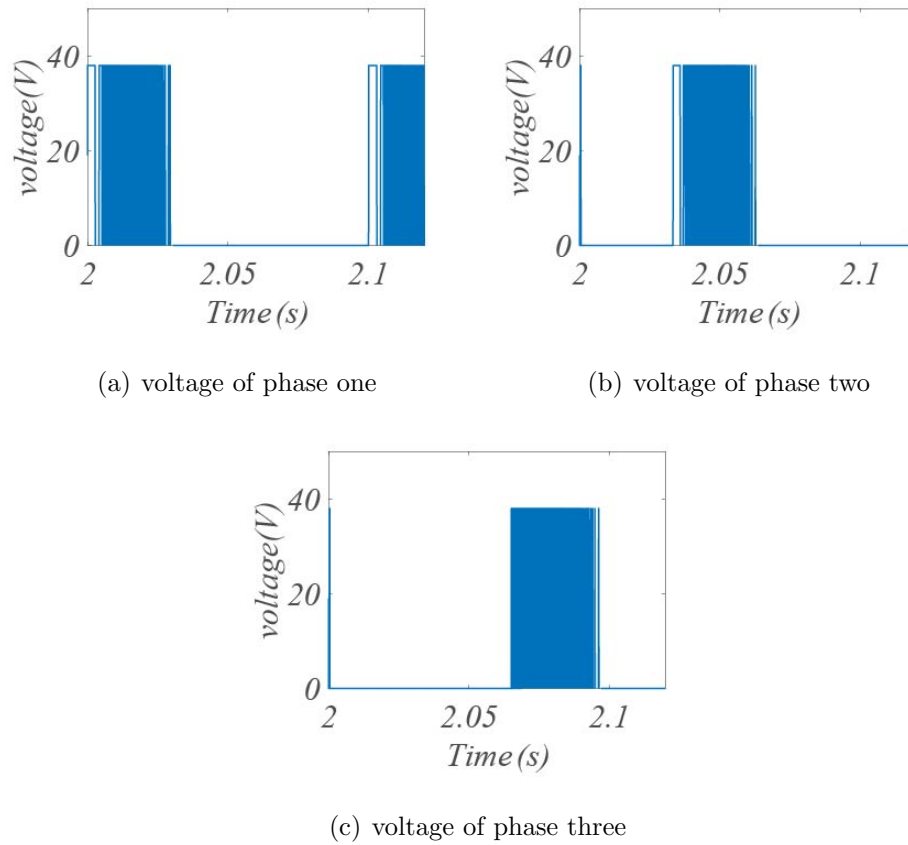
Fig. 4.10. Voltages come from the inverter

Fig. 4.12. For example, $\triangle T_1$ is the phase torque captured by the phase torque block, $\triangle T_2$ and $\triangle T_3$ are captured in the same way as it is shown in the schematic block diagram. The purpose of this diagram is to give a clear understanding of the overall layout.
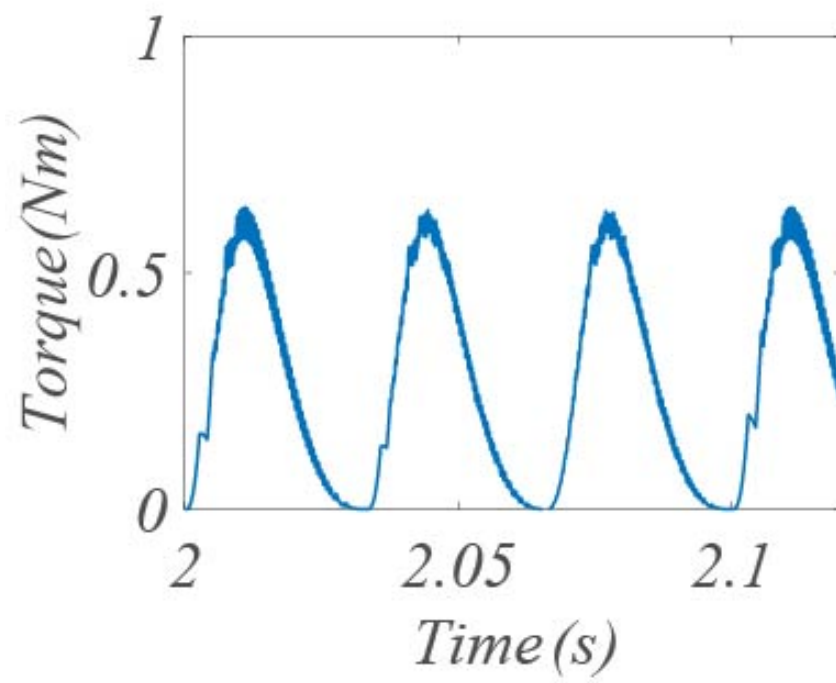
Fig. 4.11. This is the torque coming from the inverter
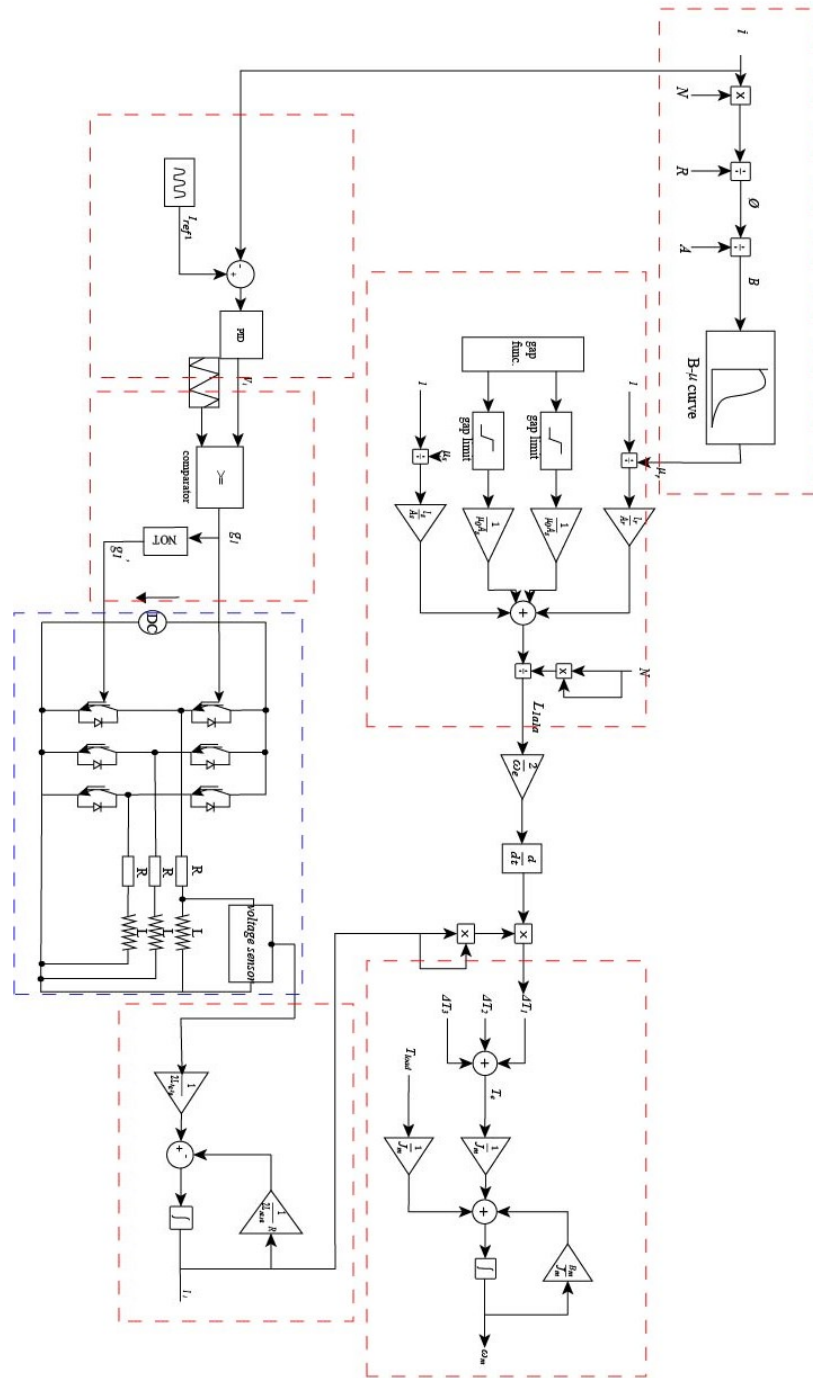
Fig. 4.12. Schematic block diagram of the SIMULINK Simulation

5. SUMMARY

In this thesis, a air-gapless motor is presented. In Chapter 1, it introduces the advantages and disadvantages of this new kind of motor when it is in the external case. In Chapter 2, according to the relationships between certain terms, simulation blocks are set up in SIMULINK environment. In Chapter 3, saturation effect is taken into counts. And by using different four kinds of coil iron. A comparison is made to improve the behavior of the motor in a future scope. In Chapter 4, a PID controller and PID tuning methods are discussed and well applied with PWM inverter, which indicates the real situation that this motor may run into in applications. This paper is devoted to bring new control strategies to explore this brand new kind of motor. Instead of avoiding rotor and stator touch each other to reduce frictions, this motor allows them to touch to increase efficiency. This motor could be competitive and be widely used in the future as long as it could increase the torque.

REFERENCES

REFERENCES

[1] M. Alibeik, O. N. M. Nezamuddin, R. M. Bagwe, M. J. Rubin, and E. C. dos Santos, "Airgapless electric motors with an external rotor," *IEEE Transactions on Industrial Electronics*, vol. 65, no. 9, pp. 6923–6935, September 2018.

[2] M. S. Trivedi and R. K. Keshri, "Predictive deadbeat current control in stationary plane for pm bldc motor drive," in *IECON 2017 - 43rd Annual Conference of the IEEE Industrial Electronics Society*, October 2017, pp. 6640–6645.

[3] A. B. F. Neves, M. V. B. de Mendona, A. d. L. Ferreira Filho, and G. Z. Rosa, "Effects of voltage unbalance and harmonic distortion on the torque and efficiency of a three-phase induction motor," in *2016 17th International Conference on Harmonics and Quality of Power (ICHQP)*, October 2016, pp. 943–948.

[4] M. F. Umar, M. N. Akbar, and S. M. R. Kazmi, "Design and simulation of a 3 phase induction motor drive based on indirect rotor field orientation using matlab simulink tool," in *2018 1st International Conference on Power, Energy and Smart Grid (ICPESG)*, April 2018, pp. 1–6.

[5] K. H. Zhao, C. F. Zhang, J. He, X. F. Li, J. H. Feng, J. H. Liu, and T. Li, "Accurate torque-sensorless control approach for interior permanent-magnet synchronous machine based on cascaded sliding mode observer," *The Journal of Engineering*, vol. 2017, no. 7, pp. 376–384, 2017.

[6] M. Luo, D. Dujic, and J. Allmeling, "Permeance based modeling of magnetic hysteresis with inclusion of eddy current effect," in *2018 IEEE Applied Power Electronics Conference and Exposition (APEC)*, March 2018, pp. 1764–1771.

[7] J. Song, S. Sung, and G. Jang, "Effect of air gap between pm segments on cogging torque and acoustic noise of bldc motor," in *2015 IEEE Magnetics Conference (INTERMAG)*, May 2015, pp. 1–1.

[8] X. Z. Xu, H. C. Feng, X. D. Wang, and B. Y. Du, "Characteristics analysis of pm linear synchronous motor with non-uniform air-gap," in *2015 IEEE International Conference on Applied Superconductivity and Electromagnetic Devices (ASEMD)*, November 2015, pp. 199–200.

[9] F. Rieger and B. Hagemann, "Mechanical shocks caused by brakes on electric motors," in *Innovative Small Drives and Micro-Motor Systems; 11th GMM/ETG-Symposium*, September 2017, pp. 1–6.

[10] K. Dutta, P. P. Puthra, and P. K. Das, "Constant torque angle controlled permanent magnet synchronous motor drive using hysteresis band current controller," in *2016 7th India International Conference on Power Electronics (IICPE)*, November 2016, pp. 1–5.

[11] R. Picatoste, M. Butcher, and A. Masi, "Current control strategy for electric motor drives using long cables," in *2017 IEEE 26th International Symposium on Industrial Electronics (ISIE)*, June 2017, pp. 257–262.

[12] K. Marouani, K. Nounou, M. Benbouzid, and B. Tabbache, "Power factor correction of an electrical drive system based on multiphase machines," in *2014 First International Conference on Green Energy ICGE 2014*, March 2014, pp. 152–157.

[13] K. Sato, J. S. Shin, T. Koseki, and Y. Aoyama, "Basic experiments for high-torque, low-speed permanent magnet synchronous motor and a technique for reducing cogging torque," in *The XIX International Conference on Electrical Machines - ICEM 2010*, September 2010, pp. 1–6.

[14] F. Copt, D. M. Araujo, C. Koechli, and Y. Perriard, "Current control strategy for dynamic winding reconfiguration of a brushless dc motor," in *2017 IEEE Energy Conversion Congress and Exposition (ECCE)*, October 2017, pp. 3577–3582.

[15] J. Wang, H. Lin, H. Li, S. Fang, Y. Huang, J. Dong, and H. Yang, "Linear representation of saturation characteristics associated with eddy currents in ferromagnetic materials," *IEEE Transactions on Magnetics*, vol. 50, no. 2, pp. 121–124, February 2014.

[16] M. Hrkel, J. Vittek, and Z. Biel, "Maximum torque per ampere control strategy of induction motor with iron losses," in *2012 ELEKTRO*, May 2012, pp. 185–190.

[17] S. Peresada, S. Kovbasa, S. Dymko, and S. Bozhko, "Maximum torque-per-amp tracking control of saturated induction motors," in *2017 International Conference on Modern Electrical and Energy Systems (MEES)*, November 2017, pp. 72–75.

[18] R. Zanasi, F. Grossi, and G. Azzone, "The pog technique for modeling multiphase asynchronous motors," in *2009 IEEE International Conference on Mechatronics*, April 2009, pp. 1–6.

[19] P. Zheng, Q. Zhao, J. Bai, B. Yu, Z. Song, and J. Shang, "Torque density improvement of transverse-flux dual rotor machine for power-split hybrid electric vehicle application," in *2014 17th International Conference on Electrical Machines and Systems (ICEMS)*, October 2014, pp. 1178–1182.

[20] P. Li, X. M. Sun, and X. Zhao, "Stabilization of linear systems with input saturation and large delay," *IEEE Transactions on Systems, Man, and Cybernetics: Systems*, pp. 1–10, 2018.

[21] M. Tajdinian, A. Bagheri, M. Allahbakhshi, and A. R. Seifi, "Framework for current transformer saturation detection and waveform reconstruction," *IET Generation, Transmission Distribution*, vol. 12, no. 13, pp. 3167–3176, 2018.

[22] N. Duan, W. Xu, Y. Li, S. Wang, Y. Guo, and J. Zhu, "Comparison of limiting loop model and elemental operator model for magnetic hysteresis of ferromagnetic materials," *IEEE Transactions on Magnetics*, vol. 53, no. 11, pp. 1–4, November 2017.

[23] H. Poritsky and J. M. Butler, "A-c flux penetration into magnetic materials with saturation," *IEEE Transactions on Communication and Electronics*, vol. 83, no. 70, pp. 99–111, January 1964.

[24] B. Baudouy, C. Berenguer, M. Takeda, J. Miller, and S. W. V. Sciver, "Void fraction effect on ac loss in saturation regime for nbti cic conductor," *IEEE Transactions on Applied Superconductivity*, vol. 9, no. 2, pp. 567–570, June 1999.

[25] M. H. S. Boloukat and A. A. Foroud, "Multiperiod planning of distribution networks under competitive electricity market with penetration of several microgrids part ii: Case study and numerical analysis," *IEEE Transactions on Industrial Informatics*, pp. 1–1, 2018.

[26] H. Yoon, P. S. Shin, and C. S. Koh, "Utilization of extended b-h curve method for consideration of 2-d magnetic properties of non-oriented electrical steels on motors," in *2010 International Conference on Electrical Machines and Systems*, October 2010, pp. 1178–1181.

[27] X. Wang, X. Su, and L. Sun, "Disturbance observer-based singularity-free trajectory tracking control of uncertain quadrotors with input saturation," in *2018 Chinese Control And Decision Conference (CCDC)*, June 2018, pp. 5780–5785.

[28] O. V. Tikhonova and A. T. Plastun, "Electromagnetic calculation of induction motor by x201c;ansys maxwell x201d;," in *2018 IEEE Conference of Russian Young Researchers in Electrical and Electronic Engineering (EIConRus)*, January 2018, pp. 822–826.

[29] C. Ma, C. Chen, Q. Li, H. Gao, Q. Kang, J. Fang, H. Cui, K. Teng, and X. Lv, "Analytical calculation of no-load magnetic field of external rotor permanent magnet brushless direct current motor used as in-wheel motor of electric vehicle," *IEEE Transactions on Magnetics*, vol. 54, no. 4, pp. 1–6, April 2018.

[30] S. M. Shakouhi, M. Mohamadian, and E. Afjei, "Rotor eccentricity fault compensation by voltage control of brushless dc motor," *IET Power Electronics*, vol. 7, no. 9, pp. 2365–2373, September 2014.

[31] T. Jonsky, H. Stichweh, M. Theeling, J. Wettlaufer, and F. Quattrone, "Modeling and parameter identification of multiphase permanent magnet synchronous motors including saturation effects," in *2015 17th European Conference on Power Electronics and Applications (EPE'15 ECCE-Europe)*, September 2015, pp. 1–10.

[32] N. Pjevalica, M. Nikolic, and N. Teslic, "Magnetic saturation of permanent magnet motor coil as key effect for initial rotor position detection," in *2015 IEEE 5th International Conference on Consumer Electronics - Berlin (ICCE-Berlin)*, September 2015, pp. 418–422.

[33] E. Levi, M. Sokola, and S. N. Vukosavic, "A method for magnetizing curve identification in rotor flux oriented induction machines," *IEEE Transactions on Energy Conversion*, vol. 15, no. 2, pp. 157–162, June 2000.

[34] O. Tikhonova, I. Malygin, and A. Plastun, "Electromagnetic calculation for induction motors of various designs by x201c;ansys maxwell," in *2017 International Conference on Industrial Engineering, Applications and Manufacturing (ICIEAM)*, May 2017, pp. 1–5.

[35] E. Levi, "Impact of iron loss on behaviour of vector controlled induction machines," in *Proceedings of 1994 IEEE Industry Applications Society Annual Meeting*, October 1994, pp. 74–80 vol.1.

[36] G. J. Park, B. Son, S. Seo, J. H. Lee, Y. J. Kim, and S. Y. Jung, "Compensation strategy of the numerical analysis in frequency domain on induction motor considering magnetic flux saturation," *IEEE Transactions on Magnetics*, vol. 54, no. 3, pp. 1–4, March 2018.

[37] A. K. Hartmann, J. Gdelhfer, R. Gottkehaskamp, and M. Pacas, "Analytical model of an inverter-fed electrically excited synchronous motor considering saturation," in *2014 International Conference on Electrical Machines (ICEM)*, September 2014, pp. 1001–1007.

[38] M. Moallem and M. Madhkhan, "Predicting the parameters and performance of brushless dc motor including saturation and slotting effects and magnetic circuit variations," in *Proceedings of 1995 International Conference on Power Electronics and Drive Systems. PEDS 95*, February 1995, pp. 509–512 vol.1.

[39] M. A. Masadeh, K. S. Amitkumar, and P. Pillay, "Power electronic converter-based induction motor emulator including main and leakage flux saturation," *IEEE Transactions on Transportation Electrification*, vol. 4, no. 2, pp. 483–493, June 2018.

[40] D. Ye, D. Yuan, M. Chen, X. Yang, and X. Zhao, "Observer-based event-triggered consensus of multi-agent systems with input saturation," in *2018 33rd Youth Academic Annual Conference of Chinese Association of Automation (YAC)*, May 2018, pp. 805–809.

[41] R. Jiayang and W. Shanming, "Estimation of saturation characteristic of induction motors by injecting sinusoidal currents with customized low frequency," in *2014 17th International Conference on Electrical Machines and Systems (ICEMS)*, October 2014, pp. 3166–3174.

[42] L. Ru and L. Ying-zi, "A kind of new simulation of electric field distribution in a pwm inverter-fed motor stator winding subjected to steep-fronted surge voltages," in *2011 6th IEEE Conference on Industrial Electronics and Applications*, June 2011, pp. 2787–2790.

[43] S. Bhandari, J. Kumar, and T. Thakur, "Tuning of pid parameters by integrated taguchi-pugh technique x2014; using region elimination approach," in *2017 IEEE International Conference on Power, Control, Signals and Instrumentation Engineering (ICPCSI)*, September 2017, pp. 1100–1105.

[44] T. M. Jahns, G. B. Kliman, and T. W. Neumann, "Interior permanent-magnet synchronous motors for adjustable-speed drives," *IEEE Transactions on Industry Applications*, vol. IA-22, no. 4, pp. 738–747, July 1986.

[45] S. Morimoto, Y. Takeda, T. Hirasa, and K. Taniguchi, "Expansion of operating limits for permanent magnet motor by current vector control considering inverter capacity," *IEEE Transactions on Industry Applications*, vol. 26, no. 5, pp. 866–871, September 1990.

[46] C. Cavallaro, A. O. D. Tommaso, R. Miceli, A. Raciti, G. R. Galluzzo, and M. Trapanese, "Efficiency enhancement of permanent-magnet synchronous motor drives by online loss minimization approaches," *IEEE Transactions on Industrial Electronics*, vol. 52, no. 4, pp. 1153–1160, August 2005.

[47] S. Noguchi, K. Suzuki, and H. Dohmeki, "The efficiency comparison by exciting waveform of the square-wave brushless dc motor," in *2015 18th International Conference on Electrical Machines and Systems (ICEMS)*, October 2015, pp. 1407–1413.

[48] A. Doerr, D. Nguyen-Tuong, A. Marco, S. Schaal, and S. Trimpe, "Model-based policy search for automatic tuning of multivariate pid controllers," in *2017 IEEE International Conference on Robotics and Automation (ICRA)*, May 2017, pp. 5295–5301.

[49] I. Ahmad, A. Voda, and G. Besanon, "Experimental validation of h x221e; siso control for high performance tunneling current measurement system and mimo extension," in *2012 IEEE International Conference on Control Applications*, October 2012, pp. 581–586.

[50] R. K. Achanta and V. K. Pamula, "Dc motor speed control using pid controller tuned by jaya optimization algorithm," in *2017 IEEE International Conference on Power, Control, Signals and Instrumentation Engineering (ICPCSI)*, September 2017, pp. 983–987.

[51] E. Flores-Morn, W. Ynez-Pazmio, and J. Barzola-Monteses, "Genetic algorithm and fuzzy self-tuning pid for dc motor position controllers," in *2018 19th International Carpathian Control Conference (ICCC)*, May 2018, pp. 162–168.

[52] I. Kecsks, E. Burkus, Z. Kirly, . Odry, and P. Odry, "Competition of motor controllers using a simplified robot leg: Pid vs fuzzy logic," in *2017 Fourth International Conference on Mathematics and Computers in Sciences and in Industry (MCSI)*, August 2017, pp. 37–43.

[53] N. E. Y. Kouba, M. Menaa, M. Hasni, B. Boussahoua, and M. Boudour, "Optimal load frequency control in interconnected power system using pid controller based on particle swarm optimization," in *2014 International Conference on Electrical Sciences and Technologies in Maghreb (CISTEM)*, November 2014, pp. 1–8.

[54] Y. Zhong, W. Xie, and X. Zhang, "A neural network compound control algorithm for complex nonlinear electric gas pressure regulating system," in *2016 Chinese Control and Decision Conference (CCDC)*, May 2016, pp. 3055–3060.

[55] Y. Chen, H. Yin, and H. Zhang, "Pid controller parameters tuning in servo system based on chaotic particle swarm optimization," in *2009 IEEE International Symposium on IT in Medicine Education*, vol. 1, August 2009, pp. 276–280.

[56] N. S. Rathore, D. P. S. Chauhan, and V. P. Singh, "Tuning of pid controller for position control of dc servo motor using luus-jaakola optimization," in *2015 International Conference on Computer, Communication and Control (IC4)*, September 2015, pp. 1–5.

[57] N. S. Rathore, V. P. Singh, and D. P. S. Chauhan, "Ise based pid controller tuning for position control of dc servo-motor using lj," in *2015 International Conference on Signal Processing, Computing and Control (ISPCC)*, September 2015, pp. 125–128.

[58] N. I. Giannoccaro, G. Manieri, P. Martina, and T. Sakamoto, "Genetic algorithm for decentralized pi controller tuning of a multi-span web transport system based on overlapping decomposition," in *2017 11th Asian Control Conference (ASCC)*, December 2017, pp. 993–998.

[59] S. Li, P. Yang, F. Yang, and G. Zhang, "On lime kiln temperature system based on ga fuzzy pid algorithm and optimal control," in *Proceedings of the 33rd Chinese Control Conference*, July 2014, pp. 4545–4550.

[60] L. Wang, X.-P. Wang, and Q.-D. Wu, "Ant system algorithm based rosenbrock function optimization in multi-dimension space," in *Proceedings. International Conference on Machine Learning and Cybernetics*, vol. 2, 2002, pp. 710–714 vol.2.

[61] O. Roeva and T. Slavov, "Firefly algorithm tuning of pid controller for glucose concentration control during e. coli fed-batch cultivation process," in *2012 Federated Conference on Computer Science and Information Systems (FedCSIS)*, September 2012, pp. 455–462.

[62] K. S. M. J. Singh, I. Elamvazuthi, K. Z. K. Shaari, and N. Perumal, "Development of pid controller tuning tool based on cuckoo search algorithms," in *2017 IEEE 3rd International Symposium in Robotics and Manufacturing Automation (ROMA)*, September 2017, pp. 1–5.

[63] Y. J. Wang, S. T. Huang, and K. H. You, "Calculation of robust and optimal fractional pid controllers for time delay systems with gain margin and phase margin specifications," in *2017 36th Chinese Control Conference (CCC)*, July 2017, pp. 3077–3082.

[64] R. R. Shukla and N. K. Patel, "Automatic generation control of an interconnected power system using energy storage units in the presence of pidf controller," in *2018 Technologies for Smart-City Energy Security and Power (ICSESP)*, March 2018, pp. 1–4.

[65] F. Mei, "The application of trail-and-error learning in c language curriculum for non-majors in computer," in *2013 8th International Conference on Computer Science Education*, April 2013, pp. 1239–1242.